1 **South African crustal fracture fluids preserve paleometeoric water signatures for up to**

2 **tens of millions of years.**

3 **Andrew W. Heard[1,*], Oliver Warr[1,2], Gaetan Borgonie[3], Borja Linage[4], Olukayode**

4 **Kuloyo[5], Jonathan W. Fellowes[6], Cara Magnabosco, Maggie C.Y. Lau[8], Mariana**

5 **Erasmus[9], Errol D. Cason[9], Esta van Heerden[9], Thomas L. Kieft[10], Jennifer C. Mabry[1],**

6 **Tullis C. Onstott[8], Barbara Sherwood Lollar[2], Chris J. Ballentine[1]**

7 **1** Department of Earth Sciences, University of Oxford, OX1 3AN, U.K.

8 **2** Department of Earth Sciences, University of Toronto, ON, M5S 3B1, Canada

9 **3** Extreme Life Isyensya, Gentbrugge, Belgium

10 **4** Consorcio de Promoción del Ovino, 49630 Villalpando, Castillo-León, Spain.

11 **5** Energy Bioengineering and Geomicrobiology Group, University of Calgary, Calgary, AB,

12 T2N 1N4, Canada

13 **6** School of Earth and Environmental Sciences, University of Manchester, M13 9PL, UK

14 **7** Flatiron Institute Center for Computational Biology, Simons Foundation, New York, NY

15 10010 U.S.A.

16 **8** Dept. of Geosciences, Princeton University, Princeton NJ 08544 U.S.A.

17 **9** Department of Microbial, Biochemical and Food Biotechnology, University of the Free State,

18 Bloemfontein, South Africa

19 **10** Biology Department, New Mexico Institute of Mining and Technology, Socorro, NM,

20 U.S.A.

21 ***** Corresponding author. Present address: Origins Laboratory, Department of the Geophysical

22 Sciences and Enrico Fermi Institute, The University of Chicago, 5734 South Ellis Avenue,

23 Chicago, IL 60637, U.S.A. (andyheard@uchicago.edu)

24

25 **Abstract**

26 Fracture fluids in Earth's crust may remain isolated for millions to billions of years, and contain

27 information on paleohydrogeology, subsurface microbial life, and conservative components

28 that help elucidate the atmospheric evolution of the early Earth. Examples include fluids in the

29 South African Kaapvaal craton which host chemolithoautotrophic microbial communities that

30 survive independent of the photosphere, and billion-year-old fluids in the Canadian Shield,

31 which preserve the Xe isotopic signature of an evolving early atmosphere. Stable isotope

32 analyses of the aqueous phase combined with isotopic analyses of the dissolved noble gases

33 provide unrivalled insight into the time-alteration history of aqueous fracture fluids. Here we

34 report stable isotope and noble gas data for fracture fluids in the Witwatersrand Basin and

35 Bushveld Igneous Province systems, South Africa. We determine closed-system radiogenic

36 noble gas residence times of 0.77-97 million years (Myr). Open-system residence times range

37 between 6.0 Kyr and 10.8 Myr. One sample from Masimong Mine has a mean closed-system

38 residence time of 85 Myr, making it one of oldest paleometeoric waters ever recorded. The δ^2H

39 and δ^{18}O of water in this sample, and in previously reported samples from the same mining

40 district that are shown to have similar ages, require an isotopically depleted source of

41 groundwater recharge. This could reflect a recharge regime at a higher paleolatitude, elevation,

42 or with higher rainfall, established up to tens of Myr ago, and perhaps similar to the recharge

43 regime in the modern Lesotho Highlands. These data suggest that groundwater isotopes can

44 provide useful paleoclimatic information for many Myr.

45

46 Keywords: noble gases; groundwater dating; crustal fracture fluids; paleohydrogeology

47

48 **1. Introduction**

49 Noble gases are powerful tracers of volatile reservoirs and physical processes in geochemistry

50 and cosmochemistry (Porcelli *et al*., 2002). Systematic variations in their solubility and

51 diffusivity, chemical inertness, and production in long-lived nuclear reactions, make noble

52 gases an analytical tool offering unparalleled insight into the timescales of transport and mixing

53 of crustal fluids (Ballentine *et al*., 2002 and references therein). Combined, noble gas and stable

54 isotope studies enable determination of the age and origins of crustal fluids by distinguishing

55 fluids that originate as recharge from the surface from fluids that are crustal-radiogenic, or even

56 magmatic in origin (Holland *et al*., 2013; Lippmann *et al*., 2003; Lippmann-Pipke *et al*., 2011).

57 The non-radiogenic dissolved noble gas composition in fluids in contact with the atmosphere

58 depends on the temperature (T) and salinity (S) of the water which equilibrates with the

59 atmosphere (Ballentine *et al*., 2002). Radiogenic noble gases are generated in the crust by the

60 decay of U, Th and K via known and quantifiable nuclear decay and secondary nucleogenic

61 activity (Ballentine and Burnard, 2002). The accumulation of non-atmospheric gas components

62 in the groundwater is controlled by the properties of the host rock, and the timescales over

63 which the water remains below the surface. Reaction and decay products may be produced *in*

64 *situ*; in the case that the fracture network is a closed system; or may be added to an open fracture

65 system by external crustal fluxes or fluid mixing as fractures open and close over geologic

66 timescales (Sherwood Lollar *et al*., 2007; Sleep and Zoback, 2007; Warr et al., 2018).

67 Radiogenic noble gases have previously been used to determine the residence times of fluids

68 sampled from the Precambrian shields of South Africa (Lippmann *et al*., 2003; Lippmann-

69 Pipke *et al*., 2011), and Canada (Holland *et al*., 2013). Fluids from the Witwatersrand basin,

70 South Africa, yielded closed system residence times of 13-170 Myr; whilst open system

71 residence times ranged from 0.6 to 23 Myr (Lippmann *et al*., 2003). Fracture fluids from 5

72 boreholes from Kidd Creek Mine, Ontario, Canada, recorded closed system residence times

73 >1.0 billion years (Gyr) (Holland *et al*., 2013; Warr *et al*., 2018). Further, the Kidd Creek Mine

74 samples contained mass-fractionated $^{124-128}$Xe, which is consistent with a model of progressive

75 fractionating Xe loss from the early atmosphere, as previously reported from fluid inclusions

76 in Archean barites and hydrothermal quartz (Pujol et al., 2009, 2011).

77 In recent years the study of fracture fluids in Precambrian cratons has revealed the existence of

78 a deep microbial biosphere, isolated from Earth's surface. A low-diversity community of

79 sulphate-reducing chemotrophic bacteria residing in fluids with radiogenic noble gas-derived,

80 open system residence times of 15.8-25 Myr were reported inhabiting 3-4 km deep, saline

81 fracture fluid from Mponeng gold mine in the Witwatersrand Basin, South Africa, in fracture

82 fluids with radiogenic noble gas-derived, open system residence times of 15.8-25 Myr (Chivian

83 *et al*., 2008; Lin *et al*., 2006). The extended fluid residence times derived from the noble gas

84 data were critical in establishing that low-diversity subsurface communities could be sustained

85 for millions of years without photosynthetic energy from Earth's surface but instead by

86 radiolytic production of both H_2 and sulphate (Lin *et al*., 2006). Fracture fluids from shallower

87 depths in South Africa and Finland that possess younger residence time estimates have yielded

88 more diverse communities (Bomberg *et al*., 2016, 2015; Borgonie *et al*., 2015; Gihring *et al*.,

89 2006; Lau *et al*., 2016, 2014, Magnabosco *et al*., 2016, 2014, Nyyssönen *et al*., 2014, 2012;

90 Pedersen *et al*., 2014; Purkamo *et al*., 2016).

91 For this study, new fracture fluids were sampled in four mines from the Witwatersrand Basin,

92 and one mine in the nearby Bushveld Igneous Complex, for major volatile, stable isotope, and

93 noble gas analysis. Previous work in the Witwatersrand Basin documented two distinct

94   hydrogeologic domains (Onstott *et al*., 2006; Sherwood Lollar *et al*., 2008; Ward *et al*., 2004).

95   The first domain mostly, but not always, occurred at depths ranging from 0.7 to 1.5 km and

96   was characterized by paleometeoric fracture fluid with intermediate salinities (0.001 to 0.1 M),

97   predominantly microbially-derived methane, and δ^2H and δ^{18}O isotopic values falling on or

98   near the Global Meteoric Water Line (GMWL) (Lippmann *et al*., 2003; Onstott *et al*., 2006;

99   Sherwood Lollar *et al*., 2006; Ward *et al*., 2004). The second hydrogeologic domain was

100   typically found at depths of 2 to 4 km and was characterized by fracture fluid with higher

101   salinities (0.1 to 3.6 M), high H_2 contents, abiogenic methane, and δ^2H and δ^{18}O isotopic values

102   located significantly above the GMWL (Onstott *et al*., 2006; Sherwood Lollar *et al*., 2006;

103   Ward *et al*., 2004). The latter isotopic signature is characteristic of Precambrian Shield brines

104   globally, and attributed to extensive alteration by water-rock interactions (Frape *et al*., 1984;

105   Fritz and Frape, 1982; Onstott *et al*., 2006). Associated with this deeper hydrogeologic domain

106   were elevated ^{21}Ne/^{22}Ne end-members interpreted to be the remnants of hydrothermal fluids

107   related to the hydrothermal metamorphic alteration of the Witwatersrand Basin sequences by

108   the Vredefort Impact at 2 Gyr ago (Lippmann-Pipke *et al*., 2011). The Bushveld Igneous

109   Complex layered mafic intrusion provides a geological setting distinct from the above studies,

110   and paleometeoric fluid has been previously reported (Gihring *et al*., 2006; Magnabosco *et al*.,

111   2014). The objective of this study is to investigate the relationships between fluid age,

112   dissolved gas contents and the extent of water-rock interaction. These relationships will

113   illuminate the timescales over which fracture fluids may preserve paleometeoric signatures

114   informative of surface climate and atmospheric composition, and the degree of

115   interconnectivity with the surface as it relates to the subsurface microbial biogeography.

116

117   **2. Geological setting**

118   **2.1 The Witwatersrand Basin**

119   The Witwatersrand Basin (Fig. 1A, 1C) is a region much-explored because of its prodigious

120   gold deposits. The basin lies within the Kaapvaal Craton, one of two continental nuclei in South

121   Africa formed approximately 3.7-2.7 Ga by episodic pulses of tectonomagmatic activity (Robb

122   *et al*., 1997; Robb and Meyer, 1995). The Archean basement rocks are comprised of granite-

123   greenstone lithologies, a combination of tonalite-tronhjemite-granodiorite gneisses and mafic-

124   ultramafic volcanic rocks and associated sediments (Robb *et al*., 1997). The Witwatersrand

125   Basin formed between 3.074-2.714 Ga (Robb and Meyer, 1995) in several discrete pulses, and

reached a maximum thickness of 7500 m. The Witwatersrand Supergroup overlies either the Archean granite-greenstone basement or the Dominion volcano-sedimentary group, which was deposited up to 3.074 Ga. Deposition in the basin was dominated by terrestrial and marginal mudstones, sandstones, and minor conglomeratic reefs. Some of the highest-grade ore occurs in organic-rich leaders which appear to be hydrothermal in origin. Sedimentation terminated when post-collisional rifting formed the overlying Ventersdorp Supergroup lavas at 2.714 Ga (Robb and Meyer, 1995).

Groundwater and exsolving gases were obtained from three gold mines in two gold mining districts of the Witwatersrand Basin. Masimong Mine lies in the Welkom district, located in the southwest portion of the basin. Here, the Witwatersrand Supergroup is overlain by 600 m of Carboniferous Karoo sediments (Tweedie, 1986). Samples were taken from within the Central Rand Group of the Witwatersrand Supergroup at Masimong gold mine at 1.9 km depth (Lau *et al.*, 2014; Magnabosco *et al.*, 2014). Tau Tona and Driefontein gold mines lie in the northwestern rim of the Witwatersrand Basin in the Carletonville mining district where the Witwatersrand Supergroup is overlain by the dolomite aquifer of the 2.60-2.55 Ga Transvaal Supergroup. At Driefontein gold mine, samples were taken within the Transvaal Supergroup at 1.046 km depth, while at the Tau Tona gold mine samples were taken from within the Central Rand Group at 3.048 km depth (Lau et al., 2014; Magnabosco et al., 2014). A fourth sample was taken from within the Central Rand Group at Star Diamonds mine at a depth of 640 m. This diamond mine is located approximately 40 km south of the Masimong gold mine, and where the Witwatersrand Supergroup is overlain by Karoo sediments and both are intersected by 124 Ma diamondiferous kimberlite (Field *et al.*, 2008; Macintyre and Dawson, 1976).

2.2 The Bushveld complex

The Bushveld complex (Fig. 1B) is the largest layered mafic intrusion in the world with the world's largest platinum group element reserves (McCandless and Ruiz, 1991). The Bushveld Complex is comprised of the Rustenberg layered mafic suite, the Lebowa granite, and Rashoop granophyre suites which intrude the 12 km thick succession of calcareous and siliciclastic sediments in the Transvaal Basin, and is overlain by the Rooiberg felsite volcanics (von Gruenewaldt *et al.*, 1985; Yudovskaya *et al.*, 2013). One fluid sample was taken at 2.1 km depth from a fracture associated with a NW-SE striking dike cutting the Rustenberg suite at

157   Zondereinde platinum mine in the far Western lobe of the Bushveld complex (Magnabosco *et*
158   *al*., 2014).

159

Material and methods

161   **3.1 Samples**

162   Samples analysed in this study were collected between March 2011 and September 2012 from
163   three gold mines (Masimong, MM51940; Driefontein, DR5IPC; and Tau Tona, TT107), a
164   diamond mine (Star Diamonds, SD15), and a platinum mine (Zondereinde, NO14) at depths
165   ranging from 640 to 3048 m (Table 1). A sterile stainless steel Margot-type plug with a multi-
166   valve sampling manifold was inserted into the borehole opening and sealed to the inner rock
167   wall or casing following the procedure of (Lau *et al*., 2014). Gas and water were flushed
168   through the apparatus to displace any air. The temperature, salinity, pH, Eh, dissolved O_2,
169   Fe^{2+}/Fe^{3+}, H_2S and H_2O_2 were measured using field probes (HANNA Instruments,
170   Woonsocket, RI USA) and Chemet kits (Chemetrics, Inc., Calverton, VA). Gas samples were
171   collected by 'gas separation' of water directed through a gas-water separator to isolate the
172   hydrocarbon rich gases from the fracture water. Gas samples were then collected by attaching
173   pre-evacuated 160 mL borosilicate glass serum vials sealed with blue butyl rubber stoppers and
174   containing 100 μL of saturated $HgCl_2$ to the gas separator or by removing the gas from the
175   separator volume and injecting it into the vials using a gas-tight syringe. Water flow rates were
176   measured from the time taken to fill a graduated bucket. Gas flow rates were similarly measured
177   from the time taken to displace a known volume of water in the gas-water separator. Noble gas
178   samples were collected by directing the exsolved gas through plastic tubing attached to three
179   50 cm long, 10 mm diameter, refrigeration-grade copper tubes connected in series with tubing.
180   After gas had flowed through the copper tubes to flush out air they were sealed using stainless
181   steel refrigeration clamps, following procedures outlined in Ballentine and Sherwood Lollar
182   (2002), or by crimper coldwelding. Water samples for isotopic analyses were collected in acid-
183   washed Nalgene bottles filled to overflowing, from a separate valve on the manifold along with
184   other water samples for geochemical and isotopic analyses following the procedure of Ward *et*
185   *al*. (2004).

186

187   **3.2 Analytical Methods**

188   *See Appendix A for full extended methods*.

189

3.2.1 Major volatile analysis

Gas and water samples were analysed for major volatiles and stable isotopes following procedures outlined by Sherwood Lollar *et al*. (2006), and Ward *et al*. (2004). Compositional analyses of gas samples were performed at the University of Toronto. Concentrations of CH_4, C_2H_6, C_3H_8, and C_4H_{10} were measured on a Varian 3400 GC equipped with a flame ionization detector. Concentrations of H_2, He, Ar, O_2, CO_2, and N_2 were measured on a Varian 3800 GC equipped with a micro-thermal conductivity detector and a Varian Molecular Sieve 5A PLOT column (25 m $\times$ 0.53 mm inner diameter). Analyses were run in triplicate and reproducibility was $\pm$ 5%.Gas composition was also determined at Princeton University for H_2, He, O_2 and N_2 (thermal conductivity detector), H_2 and CO (reduced gas detector), and CO_2 and CH_4 (flame ionization detector) by gas chromatography (Peak Performer1 series, Peak Laboratories, USA) using Ultra-High Purity (UHP) Ar as a carrier gas.

202

3.2.2 Water stable isotope analysis

Hydrogen and oxygen isotope analyses of waters were performed at the University of Waterloo. The δ^2H analyses were performed via manganese reduction at 900 ℃ using a method modified from Coleman *et al*. (1982). The $\delta^{18}O$ analyses were performed by the CO_2 equilibration method of Epstein and Mayeda (1953). Reproducibility on duplicate analyses are $\pm$ 0.4 ‰, and $\pm$ 0.1 ‰ with respect to V-SMOW for δ^2H and $\delta^{18}O$ respectively.

209

3.2.3 Noble gas analysis

Noble gas analyses were conducted following the methods of Barry *et al*. (2016) and Warr *et al*. (2018). Copper sample tubes were attached to the vacuum line and leak checked with purified He and a Hiden Analytical HAL-201 quadrupole mass spectrometer before being pumped overnight to $< 10^{-6}$ Torr. Sample gas was released by crushing of knife edges in vacuum and reactive gases were removed by sequential reaction with Ti sponge (held at 950 ℃ and then cooling to room temperature), 250 ℃ SAES GP50, and room temperature SAES NP10 getters respectively. Water vapour was removed with a stainless steel cryotrap at 180 K. Noble gases were cryogenically separated by the cycling of stainless-steel and charcoal traps

219   cooled using He compressors. A ThermoScientific Helix SFT mass spectrometer with a single
220   Faraday cup and electron multiplier was used for analysis of ^{4}He and ^{3}He respectively. Neon,
221   Ar, Kr, and Xe were released sequentially and analysed using a ThermoScientific Argus VI
222   mass spectrometer with four Faraday cups and a single electron multiplier. Sample Kr and Xe
223   were released and measured together using a combination of multicollection and peak jumping.
224   At each release step, residual noble gas from the previous step was removed by several cycles
225   of heating, re-cooling and dynamical pumping. New aliquots of available replicate samples of
226   MM51940, TT107, and NO14 were analysed for Xe isotopes on a second system optimised
227   solely for Xe (and Kr) isotope measurements with a GVI Helix MC mass spectrometer
228   equipped with 5 Faraday cups in static collection configuration, which has produced consistent
229   high-precision results in earlier publications (Holland et al., 2009, 2013). Inline gas purification
230   was performed in a similar manner to that outlined above but without cryotrapping of water.
231   Analysis of all 9 Xe isotopes was accomplished by the retention of a 20 % aliquot of the purified
232   gas by trapping on stainless steel at liquid N_2 temperatures during the analysis of ^{124}Xe, ^{126}Xe,
233   ^{129}Xe, ^{131}Xe, and ^{134}Xe. Afterwards, ^{128}Xe, ^{130}Xe, ^{132}Xe, ^{134}Xe, and ^{136}Xe were measured in
234   this 20 % aliquot with ^{134}Xe used to normalise between runs. Sample data were corrected by
235   subtraction of procedural blanks which were < 1 % on all noble gas isotopes in both mass
236   spectrometer setups. Sample data are normalised to full procedural air calibrations run
237   periodically among sample analyses for the Argus-SFT setup, or on the same day as sample
238   analysis in the GVI setup. All analytical uncertainties on noble gas measurements were
239   combined in quadrature and in the following sections these uncertainties are reported and
240   interpreted at the ± 1 σ level.

241

4. Results

4.1 Major volatiles

244   The observed gas to water ratios at sampling ranged from 0.002 to 0.2. The gas compositions
245   separated from the fracture waters were predominantly comprised of N_2 (14.7-85.6 %),
246   hydrocarbons (1.77-76.6 % CH_4, 0.002-2.80 % C_2H_6, 0.13-0.30 % C_3H_8), and O_2 (0 -21.6 %)
247   (Table 2), in addition to concentrations of percent levels of He (Section 4.3). H_2 concentrations
248   ranged from 0.0004 to 1.26 %. Samples with air-like O_2/N_2 yielded O_2 concentrations that were
249   higher than that expected from the dissolved O_2 measured at the borehole, which ranged from

250   0.06 to 0.2 ppm, suggesting that some of the gas samples had been partially contaminated by

251   air (Table 2).

252

4.2 Groundwater stable isotopes

254   Fracture waters had $\delta^{18}O$ and δ^2H from -7.00 to -4.44 ‰ V-SMOW and -40.1 to -24.3 ‰ V-

255   SMOW, respectively (Fig. 2, Table 2). The values were all significantly lighter than the mean

256   annual weighted isotopic composition of rainfall for the two GNIP stations in South Africa,

257   Pretoria with $\delta^{18}O = -3.8$ ‰ and $\delta^2H = -16.9$ ‰ and Cape Town $\delta^{18}O = -3.4$ ‰, $\delta^2H = -13.1$

258   ‰ (West *et al*., 2014). The isotopic values for Zondereinde, Tau Tona and Driefontein in the

259   north are consistent with those reported by West *et al*. (2014) for groundwater-sourced water

260   supply wells in the same area, and with previous results reported for the dolomite aquifer

261   located at Driefontein gold mine (Onstott *et al*., 2006). The isotopic values for Masimong and

262   Star Diamonds fracture water, however, are much lighter than for groundwater-sourced water

263   supply wells in the same region, where the $\delta^{18}O$ ranges from -2.9 to -4 ‰ and the δ^2H ranges

264   from -20 to -29 ‰ (West *et al*., 2014). The spatial variation in the groundwater-sourced water

265   supply wells is consistent with the $\delta^{18}O$ and δ^2H values predicted by the Online Isotopes in

266   Precipitation Calculator (OIPC, http://waterisotopes.org), indicating that the deeper fracture

267   waters from Zondereinde, Tau Tona and Driefontein have a predominantly paleometeoric

268   origin. This is consistent with the low salinity of these fracture waters (Magnabosco *et al*.,

269   2014). The light isotopic values of the Masimong and Star Diamond fracture fluids are

270   consistent with those reported for other mines in the Welkom mining district (Duane *et al*.,

271   1997; Lin *et al*., 2006). All of the Welkom fracture water data plot slightly left of the global

272   meteoric water line (Craig, 1961) and are consistent with $\delta^{18}O$ and δ^2H values predicted by

273   OPIC for the Lesotho Highlands (West *et al*., 2014; and shaded area in Fig. 2). The Lesotho

274   Highlands occur 250 km southeast of the Welkom mining district with an elevation of 2500 m

275   and an annual rainfall of 1 m compared to 1300 m elevation and 400 mm annual rainfall for

276   Welkom. This suggests that the more saline fracture fluid from Masimong gold mine and Star

277   Diamonds mine may have originated as paleometeoric water in the Lesotho Highlands or from

278   a similar hydrological regime.

279

4.3 Noble gases

Sample noble gas concentrations varied by as much as a factor of 18 on ^{20}Ne to less than 7 on ^{130}Xe (Table 1). In part this reflects the variable abundance of hydrocarbons and other major volatiles which control the dilution of noble gases in the gas phase. Hence, noble gas elemental ratios enable more effective comparison between different samples. Most samples have ^{20}Ne/^{36}Ar which range from 0.200 (MM51940) to 0.306 (NO14), and similar to air-saturated water (ASW ^{20}Ne/^{36}Ar = 0.160). Sample SD15 was more air-like with ^{20}Ne/^{36}Ar = 0.544 (air ^{20}Ne/^{36}Ar = 0.524). This sample also featured air-like ^{86}Kr/^{36}Ar = 6.02 × 10^{-3}, and ^{130}Xe/^{36}Ar = 1.03 × 10^{-4}, and has the lowest radiogenic ^{4}He/^{20}Ne and nucleogenic ^{21}Ne/^{22}Ne ratios of any sample; further indication of a dominant contribution of air. We conclude that the noble gases in this sample are dominated by air contamination. This most likely occurred during sampling because this borehole only penetrated 1 m into the fracture wall and may have aspirated some mine air through tunnel wall fractures when flowing. We note that whilst only SD15 showed evidence of major air contamination, the elemental ratios of other samples, hereafter referred to as 'uncontaminated', still have variable evidence for some air contamination (up to 22% in on NO14; Section 5.2).

Concentrations of ^{4}He ranged from 3.22×10^{-3} to 0.102 cm^{3}/cm^{3} of gas at standard temperature and pressure (STP). All samples were strongly radiogenic (Table 3), with ^{3}He/^{4}He ranging from 9.62 ± 0.36×10^{-3} to 0.114 ± 0.003 R$_A$ (Air ^{3}He/^{4}He = 1 R$_A$ = 1.40×10^{-6}; Mamyrin *et al*., 1970). The ^{3}He/^{4}He of sample gases reflects the accumulation of crustal radiogenic He (0.007 R$_A$) and demonstrates that the fracture fluids have remained isolated from the atmosphere, consistent with a paleometeoric origin (Ballentine and Burnard, 2002). Mantle He contributions are considered negligible, consistent with studies for fracture fluids in other Precambrian Shield studies (Holland *et al*., 2013; Kietäväinen *et al*., 2014; Lippmann-Pipke *et al*., 2011; Sherwood Lollar *et al.*, 1993; Warr *et al.*, 2018).

Concentrations of ^{20}Ne ranged from 6.9 × 10^{-7} to 9.0 × 10^{-6} cm^{3}/cm^{3} gas at STP. The ^{20}Ne/^{22}Ne ranged from 9.047 ± 0.007 to 10.077 ± 0.013 (Table 3; Fig. 3). The lowest value (MM51940) indicates a large addition of crustal nucleogenic ^{22}Ne to initially air-like Ne (air ^{20}Ne/^{22}Ne = 9.80; Eberhardt *et al*., 1965). The sample with a ^{20}Ne/^{22}Ne ratio higher than air (DR5IPC) falls close to the trajectory in 3-isotope space taken by a mass-dependent fractionation process such as diffusive transport. Measured ^{21}Ne/^{22}Ne values ranged from 0.0300 ± 0.0001 to 0.0643 ± 0.0003. All samples have excesses in ^{21}Ne relative to air (air ^{21}Ne/^{22}Ne = 0.0290; Eberhardt *et al*., 1965) indicating a resolvable contribution of nucleogenic ^{21}Ne.

313 Concentrations of ^{36}Ar ranged from 3.45×10^{-6} to 2.93×10^{-5} cm^3/cm^3 gas at STP, and ^{40}Ar/^{36}Ar

314 values in all samples were enriched relative to the atmospheric ratio of ^{40}Ar/^{36}Ar = 298.56 (Lee

315 *et al*., 2006). Specifically, measured ^{40}Ar/^{36}Ar values varied between 323.6 ± 0.6 and $2636 \pm$

316 5, indicating a resolvable contribution of crustal radiogenic ^{40}Ar from ^{40}K decay (Table 3). All

317 samples have ^{38}Ar/^{36}Ar similar to the atmospheric value (0.1885; Lee *et al*., 2006), ranging

318 from 0.1828 ± 0.0005 to 0.1906 ± 0.0005. The sample with the lowest ^{38}Ar/^{36}Ar, DR5IPC, also

319 had the highest ^{20}Ne/^{22}Ne ratio and is indicative of coherent mass dependant fractionation such

320 as diffusion (Zhou et al., 2005).

321 Concentrations of ^{86}Kr ranged from 3.43×10^{-8} to 2.39×10^{-7} cm^3/cm^3 gas at STP. Measured

322 isotope ratios were similar to air (^{86}Kr/^{84}Kr = 0.305; Basford *et al*., 1973).

323 Concentrations of ^{130}Xe ranged from 8.1×10^{-10} to 5.4×10^{-9} cm^3/cm^3 gas at STP (Table 5 and

324 Fig. 4). Measurements made with the Argus VI showed light isotope ratios of ^{124,126,128}Xe/^{130}Xe

325 to be within analytical uncertainty of the atmospheric value at 1 σ in all samples (^{124}Xe/^{130}Xe

326 = 0.02337; ^{126}Xe/^{130}Xe = 0.02180; ^{128}Xe/^{130}Xe = 0.4715; Basford *et al*., 1973); except sample

327 MM51940 which had a 5 % depletion in ^{126}Xe/^{130}Xe relative to the atmospheric value.

328 MM51940, TT107 and the air-contaminated SD15 featured ^{134,136}Xe excesses, which deviated

329 from air by more than 1σ. For all samples, ^{136}Xe/^{134}Xe was consistent with the predictions of

330 atmospheric Xe mixing with spontaneous ^{238}U fission products (Fig. 5, Eikenberg *et al*., 1993;

331 Wetherill, 1953). Determinations of Xe isotope ratios made on the GVI Helix MC mass

332 spectrometer for samples MM51940, TT107, and NO14, exhibited minor discrepancies

333 compared to the measurement made by the Argus VI. The depletion of MM51940 in

334 ^{126}Xe/^{130}Xe measured on the Argus VI was absent from the GVI data; all light Xe isotope

335 measurements (^{124,126,128}Xe) were air-like. The excesses in ^{134,136}Xe/^{130}Xe from Argus VI

336 measurement of TT107 were also different from the GVI results, which indicated air-like

337 isotope ratios for this sample across the isotope spectrum. The analytical error on some Argus

338 VI Xe isotope ratio measurements for TT107 and NO14 exceeded 2 %, whereas GVI

339 measurements all had < 1 % error. Due to the demonstrably higher precision of Xe isotope

340 measurements on the GVI instrument, Xe isotope ratios measured on the GVI are used for

341 samples MM51940, TT107, and NO14, whereas Argus VI measurements of Xe in these

342 samples are used to interpret Xe elemental concentration, as for all other noble gases in all

343 samples in this study. By necessity Xe isotope ratio measurements made with the Argus VI are

344 reported for those samples (DR5IPC, SD15) which did not have duplicates measured on the

345 GVI.

5. Discussion

5.1 Atmospheric noble gases in groundwater

Air-derived noble gases (e.g. ^{20}Ne, ^{36}Ar, ^{86}Kr, ^{130}Xe) are not significantly produced by crustal nuclear decay processes, therefore deviations from their estimated initial air-saturated water (ASW) concentrations track physical degassing and mixing processes. Noble gas solubility, depends on temperature and salinity at the time of water-atmosphere equilibration and increases from the light to heavy noble gases. The co-sampled waters are all less saline than seawater (Magnabosco *et al*., 2014, 2016) and we assume a meteoric origin for all groundwaters sampled in this study. The ASW reference used here is fresh 'Lake Baikal' water at 20°C (Kipfer *et al*., 2002) to be consistent withLippmann *et al*. (2003).

5.2 Initial noble concentrations in fracture fluids

Ideally, gas separation during sampling would remove all of the dissolved noble gases from the sampled fracture water. In that case and assuming a single phase pristine fluid, multiplying sample gas concentrations by measured gas to water flow rate ratios, F_g/F_w (where F_g and F_w are gas and water flow rates respectively) obtains the initial fracture water dissolved gas concentrations. Estimates made with available flow rate data (Table 6) show significant variability in atmospheric noble gas contents relative to ASW. Samples MM51940, TT107, and NO14 have ^{20}Ne contents, which are approximately 97%, 84%, and 89% of the ASW values respectively. Sample gases are also enriched in ^{20}Ne/^{36}Ar and depleted in ^{86}Kr/^{36}Ar and ^{130}Xe/^{36}Ar relative to ASW. We infer that not all gas was stripped from fracture waters during sampling, and a solubility fractionation occurred, with the lighter, less soluble noble gases being more effectively (but still incompletely) exsolved from their co-sampled waters during sample collection. As a result, the original dissolved noble gas concentrations are underestimated by the simple calculation using flow rate ratios, and we apply a model of solubility fractionation to correct for this partial exsolution, using established quantitative approaches (Ballentine *et al*., 2002 and references therein). Following the hypothesis that incomplete exsolution of noble gases to the sample gas during gas stripping, we tracked elemental compositions of a sample gas generated by different degrees of partial exsolution after generation of a headspace (in the gas-water separator), using a simple model of noble gas

377 solubility and initial fresh ASW at 20°C (Kipfer *et al*., 2002). The number of moles $[i]_g$ of gas

378 species *i* exsolved into a gas volume V_g from a volume of water V_w is calculated as

379 $$[i]_g = [i]_T (\frac{22400\ T\ \rho_{H2O}\ V_w}{18 \times 273\ \gamma_i\ K_i\ V_g} + 1)^{-1} \tag{1}$$

380 where $[i]_T$ are moles of *i* in the gas phase and total system respectively, T is temperature in K,

381 ρ_{H2O} is the density of water in g/cm^3, γ_i is the T- and salinity (S)-dependent liquid phase activity

382 coefficient of *i*, and K_i is the Henry's Law solubility constant of *i* in atmospheres (Ballentine

383 *et al*., 2002). We used a closed-system degassing model that assumes that exsolved gas enters

384 a single batch gas volume that remains in equilibrium with the parent fluid. This simulates the

385 case where some noble gas may remain dissolved in co-produced water in the gas separator if

386 gas separation was incomplete. Equilibrium degassing of fresh ASW at 20 ℃ was modelled

387 with between $V_g/V_w = 0.001$ and $V_g/V_w = 1.0$ in Equation 1. Degassing curves (Fig. 6) were

388 constructed for each sample at the T, S corresponding to measurements of co-produced water

389 (Magnabosco *et al*., 2014, 2016). Initial gas compositions show strong dependence on

390 degassing T and S, but the curves converge at higher V_g/V_w as compositions evolve towards

391 total degassing of the same initial model ASW. All sample points fall above equilibrium

392 degassing curves in [^{20}Ne] vs ^{20}Ne/^{36}Ar space, which suggests some contamination by

393 extraneous air during sampling. When extrapolated along an air-mixing line to their respective

394 degassing curves, sample data indicate produced gas/water ratios from $V_g/V_w = 0.299$ for

395 MM51940, to $V_g/V_w = 0.012$ for NO14. For comparison, the estimated volume flow rates ratios

396 recorded for these samples were $F_g/F_w = 0.235$, and $F_g/F_w = 0.017$ respectively. For comparison

397 we also display the trajectory for open-system degassing (Figure 6), wherein small gas volumes

398 in instantaneous equilibrium with the fluid are exsolved and transported away as a separate

399 phase. Gases remaining in the water are fractionated more strongly than in a closed system,

400 and ratios follow Rayleigh distillation:

401 $$([i]/[Ar])_w = ([i]/[Ar])_0\ P^{\alpha-1} \tag{2}$$

402 where $([i]/[Ar])_0$ is the initial i/Ar in the water, P the fraction of Ar remaining in the water and

403 α is the gas/liquid fractionation coefficient (Ballentine *et al*., 2002 and references therein).

404 Groundwater gas can be fractionated in this way when a free gas phase is able to escape from

405 fractures separate from the water. This process cannot have controlled the composition of a

406 bulk gas phase obtained by (incomplete) gas stripping of water within sampling apparatus.

407   Taking closed-system partial degassing of fluids during gas stripping during sampling as the
408   most reasonable scenario, a simple two-component mixing calculation was used to determine
409   air contributions. These were estimated to range from <1 % in MM51940 to approximately 22
410   % in NO14 from mixing calculations, and we anticipate that the most plausible explanation for
411   the source of these air additions is, as discussed previously, that air was incorporated during
412   sampling. The process of draining the fluids from the fractures by the mining operations cannot
413   exclude the possibility of drawing in modern mine air. If air is entrained or dissolved in portions
414   of the draining fracture fluid that is subsequently sampled this could account for the extensive
415   degree of 'air contamination' observed in the samples collected for noble gas analysis.
416   Contamination by mine air may have occurred because the seal between the fracture walls and
417   the sampling manifold was not airtight, because the sampling apparatus were not flushed with
418   fracture water and gas for a sufficiently long time to displace all air before samples were
419   collected and sealed, or because the borehole itself aspirated air; as is observed to occur
420   significantly in the Star Diamonds borehole and explains the total contamination of that sample.
421   However, whilst we consider it most likely that air was introduced in sampling rather than in
422   the laboratory (as all copper sample tubes were leak checked in the laboratory with He), the
423   atmosphere should be homogeneous with respect to non-radiogenic noble gases to the margin
424   of error we are interested in, so functionally the exact point at which an air component was
425   introduced will not affect our concentration corrections. Air contributions to each noble gas are
426   corrected for by subtracting the volume fraction of air multiplied by the concentration in air
427   from each sample and renormalized through dividing by (1 – vol% air). Dissolved
428   concentrations are then obtained by dividing air-corrected concentrations by their respective
429   degree of degassing in the closed system model, taking the ratio to the corrected [^{36}Ar], and
430   multiplying by [^{36}Ar] in ASW. The corrected ^{20}Ne/^{36}Ar and ^{86}Kr/^{36}Ar values are close to the
431   ASW values (^{20}Ne/^{36}Ar$_{ASW}$ = 0.16, ^{86}Kr/^{36}Ar$_{ASW}$ = 1.15 × 10^{-2}; Kipfer *et al.*, 2002); but
432   corrected ^{130}Xe/^{36}Ar values range from 2.30 to 4.31 × 10^{-4} around the ASW value of 3.68 × 10^{-4}
433   (Table 7). Preferential absorption of the heavy noble gases into minerals in organic rich
434   sedimentary rocks (e.g. Podosek *et al.*, 1981) may contribute to Kr and Xe enrichments in
435   groundwater interacting with these buried lithologies. In the case of NO14, which is from a
436   layered igneous complex, any interaction with organic-rich sediments would have to have
437   occurred in the surrounding country rock, either the immediately adjacent Transvaal
438   Supergroup, or the nearby Witwatersrand basin sediments themselves, before fracture fluids
439   migrated to their current location. Adsorption to sedimentary rocks could have had the opposite
440   effect of stripping some Xe from the lower temperature fracture fluids, which appear Xe-

14

441 undersaturated. Air contamination dilutes the radiogenic noble gas isotopes in fracture fluid

442 samples. Therefore, we also correct noble gas isotopic ratios using a simple two-component

443 mixing calculation like that used above for concentrations. These corrected ratios, which are

444 representative of the original fluid, are also presented in Table 7. In addition to the solubility

445 control of noble gas elemental ratios, sample DR5IPC features enrichment in $^{20}Ne/^{22}Ne$

446 depletion in $^{38}Ar/^{36}Ar$, which is consistent with a mass-dependent isotope fractionation process.

447 This phenomenon was observed previously in San Juan Coal Basin gases by Zhou *et al.* (2005)

448 and was modelled as the result of the rapid diffusion of noble gases from groundwater under

449 non-equilibrium conditions. In DR5IPC this rapid diffusive transport could have occurred

450 during gas stripping of fracture waters during sampling or as an in-fracture process.

451 Importantly, Zhou *et al.* (2005) note that whilst the process can create severe mass-dependent

452 fractionation of the light noble gas isotope ratios, elemental ratios are still overwhelmingly

453 controlled by solubility.

454

5.3 Noble gas residence times

456 We calculate closed-system and open-system noble gas residence times. The residence time of

457 a fracture fluid is the time required for the excess radiogenic noble gas (defined as the

458 concentration of noble gas in excess of that explainable by equilibration with the atmosphere

459 during recharge) to have accumulated via *in situ* and external fluxes. Excess noble gas

460 concentrations in fracture waters (in $cm^3 STP/g_{water}$) are calculated as:

461 $$[^{21}Ne^*] = [(^{21}Ne/^{20}Ne)_{Sample} - (^{21}Ne/^{20}Ne)_{ASW}] \times (^{20}Ne/^{36}Ar)_{Sample} \times [^{36}Ar]_{ASW} \qquad (3)$$

462 $$[^{40}Ar^*] = [(^{40}Ar/^{36}Ar)_{Sample} - (^{40}Ar/^{36}Ar)_{ASW}] \times [^{36}Ar]_{ASW} \qquad (4)$$

463 $$[^{136}Xe^*] = [(^{136}Xe/^{130}Xe)_{Sample} - (^{136}Xe/^{130}Xe)_{ASW}] \times (^{130}Xe/^{36}Ar)_{Sample} \times [^{36}Ar]_{ASW} \qquad (5)$$

464 where the degassing-corrected values of $(^{20}Ne/^{36}Ar)_{Sample}$, and $(^{130}Xe/^{36}Ar)_{Sample}$ are used. It is

465 assumed that essentially all ^4He is radiogenic so that $[^4He^*]$ is simply the degassing-corrected

466 $[^4He]$ given in Table 7. The values of $[^4He^*]$, $[^{21}Ne^*]$, $[^{36}Ar^*]$, and $[^{136}Xe^*]$ are given in Table

467 8.

468 It is convenient to express radiogenic noble gas excesses as concentration of atoms per gram

469 of porous host rock, in order to equate accumulation in pore waters to local production and

470 external fluxes which both depend upon radioactive decay of rock-forming elements:

471      $[i*]_{a/gr} = 2.6868 \times 10^{19} \times [i*]_{cc/gw} \times [N/(1-N)] \times (\rho_w/\rho_r)$ (6)

472   where $[i*]_{a/gr}$ and $[i*]_{cc/gw}$ are concentrations of excess noble gas $i*$ in atoms/g_{rock}, and cm^3

473   STP/g_{water} respectively, 2.6868×10^{19} is the conversion factor from cm^3 STP to molecules (in

474   this case noble gas atoms), N is bulk porosity, and ρ_w and ρ_r are the densities of the fracture

475   fluid and host rock. Based upon the salinities, the fracture fluid densities range from 1.0002 to

476   1.002 g/cm^3. The bulk densities of the Witwatersrand quartzite, Mooidrai Dolomite, and

477   Merensky Reef (Bushveld) are 2.68 ± 0.03 g/cm^3 (Silver *et al.*, 2012), 2.85 g/cm^3 (Lippmann

478   *et al.*, 2003), and 3.2 g/cm^3 (Cawthorn, 2010) respectively. The bulk porosity of the

479   Witwatersrand quartzite is 0.7 ± 0.14 % (Silver *et al.*, 2012). The porosity reported for the

480   Mooidraai Dolomite ranges from <2 % to 14 % (Vegter and Foster, 1992), and here we use a

481   value of 2 % which makes age estimates conservative. The fracture porosity is typically much

482   less than the matrix porosity in fractured metamorphic and igneous rocks (Nordstrom *et al.*,

483   1989) and could be as high as 0.05 % for heavily fractured rock to as little as 0.002 %. Here

484   we use a value of 0.05 % for porosity in the Bushveld to encompass matrix and fracture

485   porosities. Porosities reported with an associated analytical uncertainty are reflective of the

486   matrix porosity of an intact piece of rock core and are thus likely underestimate both the true

487   bulk porosity of the fractured rock system, and the uncertainty in the value of the porosity. To

488   account for this we follow the approach of Sherwood Lollar *et al.* (2014) and adopt a 45 %

489   relative uncertainty, selected to demonstrate the effect of varying estimates of porosity within

490   a wide range for crustal rocks. The resulting uncertainties on age estimates are therefore not

491   analytical error bars, but demonstrations of uncertainties in residence times in the most

492   conservative sense, which encompass both overly large and overly small values of porosity and

493   any changes that may occur with porosity change on depth and compaction over time (Warr *et*

494   *al.,* 2018).

495   The *in situ* production of ^{4}He, ^{40}Ar and ^{136}Xe in fracture host rocks is governed by the nuclear

496   decay equations:

497      $^4\text{He}* = 8 \times [^{28}\text{U}] \times (e^{\lambda_{238}\tau} - 1) + 7 \times [^{235}\text{U}] \times (e^{\lambda_{235}\tau} - 1) + 6 \times [^{232}\text{Th}] \times (e^{\lambda_{232}\tau} - 1)$ (7)

498      $^{40}\text{Ar}* = 0.105 \times [^{40}\text{K}] \times (e^{\lambda_{40}\tau} - 1)$ (8)

499      $^{136}\text{Xe}* = \lambda_{FXe}/\lambda_{238} \times [^{238}\text{U}] \times (e^{\lambda_{238}\tau} - 1)$ (9)

500   Where ^{4}He*, ^{40}Ar*, and (^{136}Xe*) are the concentrations of radiogenic (fissiogenic) noble gas

501   produced in a rock with $[^{238}\text{U}]$, $[^{235}\text{U}]$, $[^{232}\text{Th}]$, and $[^{40}\text{K}]$ concentrations in atoms/g_{rock}, over

502   time τ in yr. λ_{238}, λ_{235}, λ_{232}, and λ_{40} are the decay constants for these radioisotopes respectively

503   in yr^{-1}, 0.105 is the proportion of ^{40}K that decays to ^{40}Ar (opposed to ^{40}Ca), and $\lambda_{FXe} = 6.83 \times$

504   10^{-18} yr^{-1} is the decay constant of ^{238}U spontaneous fission events which produce ^{136}Xe (Ragettli

505   *et al.*, 1994; Steiger and Jäger, 1977). The production of nucleogenic ^{21}Ne* is calculated

506   assuming a ^{4}He/^{21}Ne* production ratio $= 2.24 \times 10^{7}$ (Ballentine and Burnard, 2002; and

507   references therein). The release factors λ_{He}, λ_{Ne}, λ_{Ar}, and λ_{Xe}, which describe the fraction of

508   radiogenic atoms which can leave the host rock and accumulate in fracture fluid, are all

509   assumed to be 1, following the approach of Holland *et al.* (2013), and therefore release of all

510   radiogenic noble gas is assumed to be quantitative.

511   Average mass concentrations U, Th and K in the host rocks of each sample are taken from the

512   published literature. These host rocks are the Merensky unit of the Bushveld at Zondereinde

513   (0.11 ppm U, 0.41 ppm Th, 0.054 % K; Lee, 1983), the Central Rand group of the

514   Witwatersrand at Masimong and Tau Tona, and the Transvaal Dolomite aquifer hosting the

515   sample from Driefontein. We use U data from representative lithologies measured in Lippmann

516   *et al.* (2003) and the Th and K concentrations from Nicolaysen *et al.* (1981). Lippmann *et al.*

517   (2003) study reported 17.6 ppm U in the Mooidraai Dolomite and U concentrations spanning

518   several orders of magnitude in the underlying Witwatersrand Supergroup. Radiogenic

519   ^{4}He*/^{40}Ar* ratios in the MM51940 and TT107 are 12, higher than the crustal average of 4.9

520   (Taylor and McLennan, 1985) indicating a source with U/K enriched relative to average crust

521   but lower than the very U-rich host rock of fluids with ^{4}He*/^{40}Ar* in the hundreds (Lippmann

522   *et al.*, 2003). We therefore use a U value of 4.7 ppm, the average of 7 selected hanging and

523   footwall samples of Witwatersrand quartzite sampled from Beatrix mine (Lippmann *et al.*,

524   2003), which is higher than the crustal average of 2.8 ppm (Taylor and McLennan, 1985). We

525   assume homogeneous radioelement concentrations in host rocks, because the fracture networks

526   are much larger than the thickness of individual stratigraphic units (Manzi *et al.*, 2012).

527   Open-system residence time calculations incorporate an additional external flux of radiogenic

528   noble gases from the underlying crust. We model this accumulation with the equation:

529    $C_i^* = 2.69 \times 10^{19} \times J_i \times \tau / \left(h \times \rho_r \times (1 - N) \right)$ (10)

530   where C_i^* is the concentration of radiogenic noble gas i in atoms/g of pore fluid-hosting rock

531   accumulated from external fluxes over time τ, J_i is the accumulation rate of noble gas in

532   cm^3/cm^2-yr in the crustal column, h is the sampling depth (cm), and ρ_r is the rock density in

533   g/cm^3 (Lippmann *et al.*, 2003). The external flux is treated here following the approach of

534   Lippmann *et al.* (2003), by assuming crustal average production of ^{4}He with the remaining

noble gases produced in relative abundances reflecting an average crustal composition (Ballentine and Burnard, 2002; Taylor and McLennan, 1985; Torgersen and Clarke, 1985).

Residence times are estimated by equating observed radiogenic noble gas excesses to the source terms (the decay equations and external fluxes) and solving for τ. Closed-system residence time estimates are independently calculated for each of the He, Ne, Ar and Xe noble gas systems (Table 8). Disagreement between age estimates from different isotope systems in each sample can indicate where the assumptions of the closed system radiogenic accumulation model break down, such as through the addition of external fluxes of noble gas, or if the release behaviour of all the different radiogenic noble gases is not quantitative. Our results show a broad range in closed-system residence times amongst samples (Table 8, Fig. 7). Sample MM51940, has residence times from 40-97 Myr (based on ^{136}Xe, ^{4}He respectively) and has a mean residence time of 85 Myr given by ^{4}He, ^{21}Ne, and ^{40}Ar. Sample TT107 has residence times from 0.77-6.1 Myr (based on ^{136}Xe, ^{21}Ne respectively) and has a mean residence time of 5.9 Myr given by ^{4}He, ^{21}Ne, and ^{40}Ar. The ^{4}He- and ^{40}Ar-derived residence times agree to within 2% and 5% of each other in MM51940 and TT107 respectively, and ^{21}Ne also gives similar residence time in each case. Additionally, MM51940 and TT107 both feature ^{136}Xe (40 and 0.77 Myr, respectively) residence times significantly lower than those given by ^{4}He, ^{21}Ne, and ^{40}Ar. Lower ^{136}Xe residence time determinations likely result from some xenon retention within the host rock which was not factored in our initial model which assumed 100 % release of Xe from the host lithology. ^{136}Xe residence times may be reconciled with the mean determination given by the other noble gas systems by assuming values of λ_{Xe} for Xe of 0.47 and 0.13 in MM51940 and TT107, respectively. For comparison, the range of values for λ_{Xe} found by Lippmann *et al.* (2003) was 0.20-1.00, so our results are consistent with previously reported inefficient Xe release in the Witwatersrand Supergroup (Lippmann *et al.*, 2003). Closed-system residence times range from 2.7-12.0 Myr (based on ^{136}Xe, ^{21}Ne, respectively) for NO14 and from 2.6-12.0 Myr (based on ^{4}He, ^{40}Ar, respectively) for DR5IPC. We do not compute ^{21}Ne ages for DR5IPC because the Ne isotopes in this sample are altered by a mass dependent isotope fractionation signal unrelated to radiogenic accumulation. This process was also observed to have fractionated ^{38}Ar/^{36}Ar in DR5IPC. Although it cannot be assessed due to the lack of a third normalizing isotope, the implied diffusive transport is expected to have affected the isotopic ratio and elemental abundance of He more severely than Ne. It would therefore be unreasonable to expect that the radiogenic noble gases in DR5IPC bear straightforward interpretation with either a simple closed- or open-system model, because

568 processes other than radiogenic accumulation have acted to alter the isotopic ratios of the light

569 noble gases in this sample. In NO14, there is a general trend towards decreasing closed-system

570 residence time estimates with increasing atomic radius, which in the context of a closed system

571 would suggest some role for inefficient release behaviour of the radiogenic noble gases from

572 minerals in the Bushveld Igneous Complex.

573 Residence times calculated with external fluxes J_i representative of average crust (Ballentine

574 and Burnard, 2002; Taylor and McLennan, 1985; Torgersen and Clarke, 1985) also show

575 diversity in fluid residence times amongst samples (Table 8). Open-system residence times

576 range from 3.4-10.8 Myr (based on ^{136}Xe, ^{4}He, respectively), in MM51940, and from 0.1-1.0

577 Myr (based on ^{136}Xe, ^{21}Ne, respectively) in TT107. In this open-system framework, residence

578 times show a generally decreasing trend with increasing atomic number, potentially indicative

579 of a mobility control on the external noble gas flux, with the lighter, more readily mobile noble

580 gases accumulating more rapidly in the fracture network. Alternatively, inefficient release of

581 Xe may explain the deficient ^{136}Xe ages, in which case there is still a mismatch in ^{40}Ar versus

582 'older' ^{4}He and ^{21}Ne residence times. This could at least in part reflect the enrichment of U/K

583 in the Witwatersrand Basin relative to average crust, which causes underestimation of the

584 external flux of noble gases from U decay (Lippmann *et al*., 2003). This is borne out by the

585 observation that the ^{4}He-derived open-system residence time (10.8 Myr) is approximately

586 twice the ^{40}Ar-derived value (4.7 Myr); while the ^{4}He*/^{40}Ar* ratio in the sample (12.1) is

587 roughly double the upper crustal average value (4.9; Taylor and McLennan, 1985). Open-

588 system residence times range from 6.0-47 Kyr (based on ^{40}Ar, ^{21}Ne respectively) for NO14 and

589 from 200-690 Kyr (based on ^{40}Ar, ^{4}He respectively) in DR5IPC. In both cases, ratios of ^{4}He,

590 (^{21}Ne,) and ^{136}Xe residence times to ^{40}Ar residence times are higher than those from closed-

591 system calculations for the same samples, which implies that average crustal values for the

592 external fluxes of noble gases are inappropriate in crustal lithologies enriched in U/K. This is

593 the case for NO14 even though the host Bushveld Igneous Complex lithology is not enriched

594 in U, unlike Witwatersrand Basin sediments. This suggests that the external flux of noble gases

595 to NO14 was at least partially sourced from surrounding sedimentary lithologies and provides

596 strong evidence for the open-system accumulation scenario for this sample. As with the closed-

597 system interpretation, the much higher residence time determinations from the light noble gases

598 ^{4}He, and ^{21}Ne in NO14 again could result in part from greater mobility of these noble gases

599 either at the local (*in situ*) or regional (external flux) scale, and incomplete release of the heavier

600 noble gases from rock into porewater.

19

601 Samples contain active ^{14}C in DIC at concentrations ranging from ~2 (MM51940) to over 50%

602 (NO14) of the modern atmospheric value (Table 9; Magnabosco *et al.*, 2014; Simkus *et al.*,

603 2016). Radiogenic noble gas ages indicate these samples should be ^{14}C-dead. In Appendix B,

604 we show that numerous plausible pathways exist for introducing ^{14}C in the small quantities

605 observed in MM51940 naturally or during sampling, whereas ^{14}C ages taken at face value are

606 irreconcilable with large observed radiogenic noble gas excesses (Table 9; Appendix). Higher

607 ^{14}C in TT107 implies a significant young water contribution, in support of combined evidence

608 from $\delta^2 H$ and $\delta^{18}O$, salinity, and Ne isotopes.

609

5.4 Paleohydrological implications

610

611 Estimates of residence time provide important context when interpreting the processes

612 occurring in the fracture fluid environment. Sample TT107 provides one example of how

613 residence times aid in understanding fluid systematics. Ne isotopes in this sample fall along an

614 evolution line previously associated with 2 Ga metamorphic fluids, and fluids which have

615 undergone extensive alteration through water-rock reaction and are generally enriched in H_2

616 and hydrocarbons (Lippmann-Pipke *et al.*, 2011). However, even our oldest residence time

617 estimates indicate that the bulk TT107 fluid is far younger than this highly altered component,

618 and it contains significant active ^{14}C. In addition, TT107 $\delta^2 H$ and $\delta^{18}O$ fall near the GMWL

619 and salinities are low and close to those of the source aquifer (Simkus *et al.* 2016), in contrast

620 with the signature anticipated for a ^{21}Ne-enriched 2 Ga hydrothermal component (Lippmann-

621 Pipke *et al.*, 2011). The aggregated signals indicate mixing between an old metamorphic fluid

622 potentially dating to 2 Ga, which carries high concentrations of radiogenic noble gas and

623 anomalously enriched ^{21}Ne, with fresh groundwater recharge. The margins of Jean's dyke,

624 which intersects the TT107 fracture network, could act as a conduit for fresh young meteoric

625 water enabling admixture of the ancient and modern fluids in TT107 (Simkus *et al.* 2016).

626 The closed-system calculation shows that MM51940 has retained a paleometeoric water

627 isotope signature over several tens of Myr isolated in the crust (Figs. 2, 7). A mean residence

628 time of 85 Myr, and individual ^4He and ^{40}Ar ages of 97 and 95 Myr respectively, would make

629 this, to our knowledge, one of the oldest paleometeoric waters ever discovered. Water-rock

630 interaction, or mixing with waters that have undergone such interaction, can move

631 paleometeoric waters away from the GMWL. Groundwaters from other Precambrian shields

632 show evidence of such water rock interaction in being highly saline and with $\delta^2 H$ and $\delta^{18}O$ that

lie above the GMWL. These characteristics reflect water rock reactions such as the alteration of feldspars to clay minerals (Fritz and Frape, 1982; Ward *et al*., 2004; Warr *et al*., 2018). There is no such altered component in fracture fluids sampled near the Masimong gold mine which could be added to MM51940 fluids (Onstott *et al*., 2006), so the upper age limit for retention of the paleometeoric signature should only depend on the time required to for the fluid to reach a sufficient crustal depth such that ambient temperatures enable isotopic equilibration between water and rock. Evidently in favourable cases paleometeoric water signatures can evade such alteration for timescales approaching 100 Myr; and equally prolonged contact with water in fractures by no means guarantees that crustal rocks will undergo appreciable water-rock reaction. This finding could extend the geological timescales for which groundwater isotopes have the potential to yield useful paleoclimatic information.

Rainfall in the Witwatersrand at the time that MM51940 groundwaters were infiltrating was ^{2}H- and ^{18}O-depleted relative to the present (IAEA/WMO, 2002). It is widely observed that precipitation becomes progressively depleted in ^{2}H and ^{18}O with higher altitude, higher latitude, increasingly continentality, higher rainfall, or under cooler climatic conditions (Dansgaard, 1964; Rozanski *et al*., 1993). Paleogeographic reconstructions for Gondwana place South Africa at higher southern latitudes than its current location throughout the Mesozoic and early Cenozoic, and its location within the Gondwana supercontinent implies an enhanced continental effect on precipitation (Besse and Courtillot, 1988; Scotese *et al*., 1999; Torsvik and Cocks, 2013; Torsvik and van der Voo, 2002). Furthermore, a mean age of 85 Myr for MM51940 groundwater roughly coincides with the beginning of a proposed phase of rapid uplift and erosion of the South African Plateau, which was associated with a sharp transition from semiarid to very humid conditions beginning around 85 Ma and persisting until the late Eocene (*ca.* 40 Ma), potentially due to the change in orography brought about by plateau uplift, and enhanced rainfall (Braun *et al*., 2014). All the above effects would deplete precipitation in ^{2}H and ^{18}O, as is observed in MM51940 paleometeoric water. We recalculate closed-system ^{4}He, ^{40}Ar, and ^{136}Xe residence times for another sample from Masimong mine, MM51870, and several samples from Beatrix mine, all of which also derive from the Welkom district and are also on the GMWL with strongly depleted in ^{2}H and ^{18}O consistent with similar recharge conditions to MM51940 (Fig. 2; Table 10; Lippmann *et al*., 2003; Lippmann-Pipke *et al*., 2011; Onstott *et al*., 2006). Residence times were recalculated using noble gas data from Lippmann *et al*. (2003), and Lippmann-Pipke *et al*. (2011) and otherwise identical model parameters to those used for MM51940 (Table 10). All recalculated residence times show agreement between

666 [4]He and [40]Ar, demonstrating the robustness of this consistent approach to residence time
667 calculations, and have deficient [136]Xe ages indicating release factors between 0.22-0.54,
668 consistent with data reported herein and with the earlier calculations of Lippmann *et al*. (2003).
669 Mean residence times range from 39-121 Myr. The oldest sample BE325 is older than
670 MM51940 and the hypothesised date of plateau uplift around 85 Ma; however model
671 uncertainties are large, and interlocational variability in the radiogenic source parameters are
672 not considered. All other samples are consistent with duration of the inferred humid
673 paleoclimate period (Braun *et al*., 2014). Sample MM519870 is younger than MM51940, with
674 a mean age of 73 Myr; which is consistent with the fracture fluid being sampled at a slightly
675 shallower depth of 1.88 km. These data do not exclusively require an interpretation of Late
676 Mesozoic-Early Cenozoic recharge, because similarly depleted water is sourced from relatively
677 recent recharge in the Lesotho Highlands where higher elevations and greater annual rainfall
678 create precipitation isotopically depleted with respect to ^{2}H and ^{18}O (West et al., 2014; Fig. 2).
679 However, coupled with coherent closed-system residence times, these data indicate that
680 paleometoric groundwaters in the Welkom district record the establishment of an isotopically
681 depleted groundwater recharge regime following uplift of the South African plateau. This
682 regime has apparently persisted to the modern day in the erosionally-resistant remnant of the
683 high plateau which the Lesotho Highlands represent.

684

685 **6. Conclusions**

686 Exsolved gases and co-sampled waters have provided us data which revealdiverse histories
687 for a suite of crustal fracture fluids. Estimated closed-system residence times from multiple
688 independent noble gas systems ranged from 0.77 to 97 Myr depending on the site. ^{136}Xe
689 persistently gives the youngest age determinations agreeing with previous studies that
690 highlight the inefficient release of fissiogenic Xe from host rocks into groundwater, relative
691 to the lighter noble gases. Open-system noble gas residence times ranged from 6.0 kyr -10.8
692 Myr. With a mean closed-system residence time of 85 Myr, sample MM51940 is to our
693 knowledge among the oldest paleometeoric waters ever recorded. We suggest that water
694 isotopes could provide a useful source of paleoclimatic information for timescales
695 approaching 100 Myr. A first order interpretation of δ^2H and δ^{18}O in this sample implies a
696 depleted moisture source relative to the modern mean as a result of various paleoclimatic and
697 paleogeographic factors. A reconsideration of noble gas data in similarly depleted

698   paleometeoric fluids sampled in the same mining district as MM51940 indicates a range of

699   closed-system residence times which encompass the age of MM51940 and are consistent with

700   an inferred period of uplift and increased humidity and rainfall in the South African plateau.

701   These data record the establishment of a high-elevation groundwater recharge regime, a

702   remnant of which has perhaps persisted in the Lesotho Highlands through to the modern day.

703

Acknowledgements

716

<u>Figure Captions</u>

718   **Figure 1** – A: Simplified geological map of the Witwatersrand Basin, after Reimold et al.

719   (1995). Coloured circles show locations of mines from where samples were collected

720   (Masimong – green; Tau Tona – purple; Star Diamonds – yellow; Driefontein – blue). B:

721   Simplified geological map of the Western Lobe of the Bushveld Complex, South Africa, after

722   Yudovskaya et al. (2013). The red circle marks the location of Zondereinde, which is

723   approximately 200 km North of Johannesburg and the Witwatersrand.

724   **Figure 2** – Stable O and H isotope ratios in South African fracture water. Coloured circles

725   represent individual sample sites (Masimong – green; Zondereinde – red; Tau Tona – purple;

726   Star Diamonds – yellow; Driefontein – blue). Greyed out data points are for previously

727   measured samples from the Welkom District (Beatrix mine, Lippmann et al., 2003 – squares;

728   Masimong mine at 1.88 km depth, Onstott et al. 2006 – diamond) The black diamond

729   represents the time averaged modern precipitation in Pretoria (IAEA/WMO, 2002). The

730   dashed line is the global meteoric water line (GMWL; Craig, 1961), the solid line is the local

731   meteoric water line (LMWL; IAEA/WMO, 2002), and the dashed and shaded area is the

732   range of values predicted from the OIPC for the Lesotho Highlands (West et al., 2014)

733   **Figure 3** – Ne isotope ratios in fracture water gases. Coloured circles representing samples are

734   as for previous figures, and 1 σ error bars are smaller than the symbols. The black diamond is

735   air. Greyed out squares are data for South African fracture waters which show anomalous

736   enrichment in nucleogenic 21Ne (Lippmann-Pipke et al., 2011). The solid line is the modern

737   crustal production trend (Kennedy et al., 1990), the short-dashed line is the South African

738   Archean crustal production trend (Lippmann-Pipke et al., 2011), and the long-dashed line is a

739   mass fractionation line (MFL) for diffusive gas loss.

740   **Figure 4** – Xe isotope ratios in fracture water gases, expressed as per mil (‰) deviations from

741   air relative to 130Xe. Coloured circles representing samples are as for previous figures, and

742   error bars are 1 σ. The green dashed line indicates the 238U fission spectrum for a 136Xe

743   excess equal to that measured in the sample from Masimong.

744   **Figure 5** – Excesses in fissionogenic 134Xe and 136Xe. Coloured circles representing samples

745   are as for previous figures, and error bars are 1 σ. The black diamond is air. The solid lines are

746   Mixing lines between air 238U fission end members (steeper line - Eikenberg et al., 1993;

747   shallower line – Wetherill, 1953).

748   **Figure 6** – Ne concentrations vs. 20Ne/36Ar in fracture water gases. Coloured circles

749   representing samples are as for previous figures, and error bars are 1 σ where larger than

750   symbols. The black diamond is air. Coloured solid lines are closed system degassing trends for

751   ASW at T and S conditions at which the sample with the corresponding colour was collected.

752   For reference the open system degassing curve for Tau Tona sampling conditions (52.1 °C and

753   0.0058 M salinity) is shown as a purple dotted line, however sample collection procedure

754   makes open system degassing extremely unlikely. Dashed lines represent mixing between air

755   and the partially exsolved gas composition which best matches sample data. Degassing and air

756   mixing trends are not shown for the sample from Star Diamonds mine because the signal for

757   that sample is dominated by air contamination.

758   **Figure 7** – Closed-system radiogenic noble gas residence times for South African fracture

759   waters. Coloured circles representing samples are as for previous figures. A: Masimong. B:

760   Tau Tona. C: Zondereinde. D: Driefontein. Error bars incorporate a 45 % uncertainty in the

761   fracture porosity model, selected to demonstrate the effect of varying estimates of porosity

762   within a wide range for crustal rocks, and hence demonstrate the most conservative sense of

763   residence time estimates.

764

765   **Appendix A**

766   **Analytical methods**

767   **Major volatiles**

768   Gas and water samples were analysed for major volatiles and stable isotopes following

769   procedures outlined by Sherwood Lollar *et al*. (2006), and Ward *et al*. (2004). Compositional

770   analyses of gas samples were performed at the University of Toronto. Concentrations of CH_4,

771   C_2H_6, C_3H_8, and C_4H_{10} were measured on a Varian 3400 GC equipped with a flame ionization

772   detector. Hydrocarbons were separated on a J and W Scientific GS-Q column (30 m $\times$ 0.32 mm

773   inner diameter) with a helium gas flow and temperature programme: initial 60 ℃ hold 2.5 min,

774   increase to 120 ℃ at 5 ℃/min. A Varian 3800 GC equipped with a micro-thermal conductivity

775   detector and a Varian Molecular Sieve 5A PLOT column (25 m $\times$ 0.53 mm inner diameter)

776   was used to determine concentrations of H_2, He, Ar, O_2, CO_2, and N_2. To determine Ar, O_2,

777   and N_2 concentrations the helium gas flow rate was 3 mL/min and the temperature program

778   was: initial 30 ℃ hold 6 min, increase to 80 vC at 15 ℃/min, hold 4 min. For CO_2 concentration

779   the helium gas flow rate was 50 ml/min and the temperature program was: initial 60 ℃, increase

780   to 250 ℃ at 20 ℃/min, hold 6 min. For H_2 and He concentrations, the argon gas flow rate was

781   2 ml/min and temperature program was: initial 10 ℃ hold 10 min, increase to 80 ℃ at 25

782   ℃/min, hold 7 min. Analyses were run in triplicate and reproducibility was $\pm$ 5%.

783   Gas composition was also determined at Princeton University for H_2, He, O_2 and N_2 (thermal

784   conductivity detector), H_2 and CO (reduced gas detector), and CO_2 and CH_4 (flame ionization

785   detector) by gas chromatography (Peak Performer1 series, Peak Laboratories, USA) using

786   Ultra-High Purity (UHP) Ar as a carrier gas.

787

788   **Water stable isotopes**

789   Hydrogen and oxygen isotope analyses of waters were performed at the University of

790   Waterloo. The δ^2H analyses were performed via manganese reduction at 900 ℃ using a method

791   modified from Coleman *et al*. (1982). The $\delta^{18}O$ analyses were performed by the CO_2

792   equilibration method of Epstein and Mayeda (1953). Reproducibility on duplicate analyses are

793     $\pm$ 0.4‰, and $\pm$ 0.1‰ with respect to V-SMOW for δ^2H and $\delta^{18}O$ respectively.

794

795   **Noble gas analysis**

796   In the laboratory, for noble gas analysis, sample tubes were attached to the vacuum line and

797   pumped overnight to a pressure of $<10^{-6}$ Torr. Seals between the line and sample passed leak

798   checks utilising purified helium and a Hiden Analytical HAL-201 quadrupole mass

799   spectrometer. Samples were opened by crushing of knife edges in vacuum to release sample

800   gas to the line. Sample gas was expanded to a calibrated volume and diluted by volume

801   expansion. Following the methods of Barry *et al*. (2016) and Warr *et al*. (2018), active gases

802   were removed by reaction for 15 minutes with titanium (Ti) sponge at 950ºC. Hydrogen was

803   removed by cooling the Ti sponge toward room temperature for 20 minutes. Remaining active

804   gases were removed by reaction for 15 minutes with hot SAES GP50 and cold SAES NP10

805   getters held at 250 ºC and room temperature respectively. Residual water was removed in a

806   stainless-steel trap held at 180 K. Cryogenic separation of noble gases was performed using

807   stainless steel and charcoal traps cooled using He compressors. The heavy noble gases (Ar, Kr,

808   and Xe) were trapped on stainless steel at 20 K for 15 minutes. The light noble gases He and

809   Ne were then trapped on charcoal at 20 K for 15 minutes. The charcoal was heated to 31 K to

810   release He to a second preparation line, and dilutions were performed with calibrated volumes.

811   Sample He was analysed using a ThermoScientific Helix SFT mass spectrometer with a single

812   electron multiplier and a single Faraday cup. After He analysis any residual trace He was

813   removed by 4 cycles of heating the charcoal trap to 50 K, cooling to 31 K, and dynamically

814   pumping. Sample Ne was released by heating the charcoal trap to 90 K for 15 minutes, and

815   analysed in a ThermoScientific Argus VI mass spectrometer with four Faraday cups and a

816   single electron multiplier. Masses 40 and 44 were also measured by simultaneously peak

817   jumping to correct for interference of doubly charged ^{40}Ar and $^{12}C^{16}O_2$ with ^{20}Ne and ^{22}Ne

818   respectively. Sample Ar was released from the stainless-steel trap by heating to 52 K and inlet

819   to the Argus VI. Any residual trace Ar was removed from the trap using 4 cycles of heating to

820   70 K, cooling to 52 K and dynamic pumping. Sample Kr and Xe were released by heating the

821   stainless-steel trap to 200 K for 15 minutes, and inlet to the Argus VI where they were measured

822   using a combination of multicollection and peak jumping.

Procedural blanks were measured using the same procedure but with no gas released to the line. Sample data are corrected by subtracting the blank measurements, which were <1 % on all noble gas isotopes. Sample data are normalised to full procedural air calibrations run periodically among sample analyses, to determine the sensitivity and discrimination of mass spectrometry. Procedural air calibrations made use of an air cylinder collected in University Parks, Oxford, UK on November 24, 2014 (Temperature: 4°C, humidity: 95%, pressure: 1027hPa). Samples were tied to recent procedural air calibrations by observed consistency in daily automated air calibrations run overnight after sample analyses.

Fresh aliquots of samples with available replicates (MM51940, TT107, NO14) were analysed for Xe isotopes on a second system optimised solely for Xe (and Kr) isotope measurements which has produced consistent high-precision results in a number of earlier publications (Holland et al., 2013, 2009). Sample tubes were loaded, opened and reacted with hot and cooling Ti as described for the Argus-SFT dual setup above. The last active gases were removed by reaction for 15 minutes with a SAES GP50 getter at 250 ºC. Sample Xe was purified using a stainless-steel trap cooled by immersion in liquid nitrogen. Purification consisted of 5 cycles of freezing, dynamically pumping, thawing, and refreezing, each for 3 minutes, to reduce the fraction of highly abundant Ar adsorbed along with Kr and Xe, all while exposed to a SAES NP10 getter held at room temperature. Purified Xe was inlet to a GVI Helix MC mass spectrometer equipped with 5 Faraday cups in static collection configuration. Five isotopes of Xe; ^{124}Xe, ^{126}Xe, ^{129}Xe, ^{131}Xe, and ^{134}Xe were measured in a first run. Approximately 20 % of sample gas was retained in order to analyse the remaining Xe isotopes; ^{128}Xe, ^{130}Xe, ^{132}Xe, and ^{136}Xe; and ^{134}Xe was measured again to be used as a normalising isotope between runs. Static collection with Faraday cups and the larger sample volumes input to the GVI mass spectrometer should provide more precise Xe isotope ratio measurements than those made by peak jumping with the Argus VI, in what represents a new application for that instrument in the lab.

Procedural blanks were performed using the same procedure but with no gas released to the line. Blank measurements were irresolvable against background voltage fluctuations in the mass spectrometer, indicating the primary blank source was electrical noise. This is accurately corrected for in our data by subtraction of baseline voltages measured at the start of sample analysis. Sample data were normalised to procedural air calibrations performed every day on the same day as sample analysis. These procedural air runs did not make use of the Ti sponge getter but were otherwise identical to sample runs. One air standard showed significant

856 deviation from air, so the sample data from that day are normalised to the mean of the remaining

857 air calibrations made during the analysis window, and uncertainties are adjusted accordingly.

858 All analytical uncertainties on noble gas measurements were combined in quadrature and in

859 following sections these uncertainties are reported and interpreted at the $\pm 1\,\sigma$ level.

860

861 **Appendix B**

862 **Consideration of active ^{14}C in apparently ancient samples**

863 All samples dated in this study contain active ^{14}C (Table 9; Magnabosco et al., 2014; Simkus

864 et al., 2016). In consideration of closed- or open-system age estimates derived from the

865 radiogenic noble gases, these fluids would in the simplest case be expected to be radiocarbon

866 dead. There are a few possible sources of live ^{14}C within the samples analysed. The first is that

867 the system is open to a source of recharge from a more modern fluid, and that an external flux

868 of radiogenic noble gases larger than the crustal average accounts for the radiogenic noble gas

869 content. Similarly, an ancient fluid that has some modern water admix might account for the

870 observation of low levels of active ^{14}C. A further possibility is that there is a modern air

871 contribution to the ^{14}C, dissolved into the fluids prior to analysis. Finally, the it has been

872 suggested that in old enough fracture systems, low levels of ^{14}C may accumulate through

873 subsurface secondary nuclear reactions (Andrews *et al*., 1989). In such a case, ^{14}C is not

874 reflective of the fluid residence time in the way it is traditionally used. We cannot rule out this

875 exotic pathway, however in the following discussion it is not treated quantitatively in any way

876 and we do not consider it to be strictly necessary.

877 Taking the model ^{14}C age for each sample at face value we determine the external flux of noble

878 gases required to reconcile the dating systems in the open system model (Table 9). We find

879 that all samples require external fluxes of both ^{4}He and ^{40}Ar greater than average upper crustal

880 values (3.6×10^{-6} and 7.3×10^{-7} cm^{3}STP cm^{-2} yr^{-1} respectively; Taylor and McLennan, 1985;

881 Torgersen and Clarke, 1985). This result is most pronounced in samples MM51940 and TT107,

882 where ^{4}He fluxes 210-850 times, and ^{40}Ar fluxes 85-340 times the upper crustal average are

883 required to satisfy respective model ^{14}C$_{DIC}$ age estimates of 32.1, and 1.41-5.68 kyr respectively

884 (Simkus et al., 2016). The magnitudes of the required crustal fluxes, for MM51940 and TT107

885 are so large that we also consider how higher local U and K concentrations could offset the

886 need for such a large open-system source term. This approach is entirely reasonable for U,

887 which can range up to 1000's of ppm in selected Witwatersrand lithologies (e.g. Lippmann et

888 al., 2003; Silver et al., 2012), but K concentrations impose an inflexible constraint on the local

889 production term. For example, if external flux J_{40Ar} is held at the average upper crustal value,

890 then to satisfy model ^{14}C age constraints, in situ K concentrations are required to be several

891 hundreds to several thousands of times larger than the literature values we use (Table 9), a

892 result which is nonsensical and thus provides a strong argument against such a scenario and

893 indicates that ^{14}C in these sample does not straightforwardly reflect an open-system residence

894 time.

895 We next consider an end-member mixing scenario where a young water component contains

896 essentially modern ^{14}C and the DIC concentrations in both components are assumed to be equal

897 and dominated by atmospheric recharge. Δ^{14}C of fracture fluid DIC (MM: -981.7 ‰; TT: -

898 496.6 ‰; NO: -417.2 ‰; DR: -930.0 ‰) was used to calculate the proportion of ^{14}C-active

899 modern water incorporated in each sample (MM: 1.8 %; TT: 50.3 %; NO: 58.3 %; DR: 7.0 %).

900 The simple mixing calculation indicates that young ^{14}C-active water should dilute radiogenic

901 noble gas excesses leading to an underestimation of closed- or open-system residence times.

902 The effect should scale with the size the young water contribution, with less than 2% young

903 water contribution to MM51940 resulting in an underestimate by less than 2 Myr in closed-

904 system and 0.2 Myr in open-system calculations respectively; small uncertainties easily

905 encompassed by the error bars of residence time calculations; whilst sample TT107 and NO14,

906 a young water contribution of more than 50% indicates noble residence times could be

907 underestimated here by over a factor of 2. Such a large contribution of young water in the two

908 latter samples will be similarly reflected in the water stable isotope ratios and salinities. Young

909 water will have shifted sample δ^2H and δ^{18}O approximately towards modern mean precipitation

910 and diluted the more saline waters of the old fluid end-member. Indeed, in the case of TT107,

911 δ^2H and δ^{18}O fall near the GMWL and salinities are low and close to those of the source aquifer

912 (Simkus *et al.* 2016), a result that is surprising given its ^{21}Ne enriched signature, which has

913 been associated with a 2 Ga hydrothermal component. The margins of Jean's dyke, which

914 intersects the TT107 fracture network acts as a conduit for fresh, young meteoric water

915 enabling admixture of the ancient and modern components in TT107 (Simkus *et al*. 2016). We

916 cannot rule out such a scenario in the case of other samples but note that it is less obvious how

917 to introduce a small proportion of modern fluid to depth a system that has otherwise retained a

918 closed system noble gas mean residence time up to many tens of Myr, unless the introduction

919 of small amounts of modern water is related to onset of mining or sampling activity. Even in

920   this case, the mixing model suggests that noble gas residence times calculated are conservative

921   and represent minimum values.

922   The process of draining the fluids from the fractures by the mining operations cannot exclude

923   the possibility of drawing in modern mine air. If air is entrained or dissolved in portions of the

924   draining fracture fluid that is subsequently sampled this could account for both the extensive

925   degree of 'air contamination' observed in the samples collected for noble gas analysis and the

926   ^{14}C activity observed; and have no effect on the radiogenic closed system noble gas mean

927   residence estimates.

928   We considered the effect of air contamination in water DIC samples equal to the air addition

929   calculated from exsolved noble gas samples. The %air contamination from noble gas samples

930   multiplied by measured gas flow rates give an estimate of the relative volumetric rate of air

931   addition to the system:

932    $F_{air} = F_{gas} \cdot x_{air}$ (1)

933   where F_{air}, F_{gas} are the flow rates of contaminating air and groundwater-exsolved gas,

934   respectively, in L/min, and x_{air} is the volume fraction of air contamination.

935   The partial pressure of CO_2 in air is 400 ppm or 4×10^{-4} atm. By the ideal gas low, the number

936   of moles of CO_2 per liter of air is:

937    $M_{CO2}^{air} = 4 \cdot 10^{-4} / (R \cdot T)$ (2)

938   where R is Gas Constant $= 8.206 \times 10^{-2}$ L atm/K/mol and T is the temperature in K.

939   From here, the moles per liter addition of modern CO_2 to sample groundwater is calculated as:

940    $M_{CO2} = F_{air} \cdot M_{CO2}^{air} / F_w$ (3)

941   where M_{CO2} is in mol/L (M) and F_w is the measured water flow rate in L/min.

942   The amount of added CO_2 that will dissolve into the sample water and be recorded as DIC is:

943    $M_{CO2}^{dis} = M_{CO2} \cdot \left(1 - \left(\frac{22400 \cdot \rho_w \cdot T \cdot F_w}{1000 \cdot 273 \cdot K_{CO2}^{m} \cdot F_{air}} + 1 \right)^{-1} \right)$ (4)

944   where ρ_w is the density of the sample water in g/cm^3, and K_{CO2}^{m} is the molar form of the

945   Henry's Law constant for the dissolution of CO_2. The result is in units of M and thus its

946   contribution to the overall DIC of sample waters can be compared directly.

At such lower air/water mixing ratios, over 99% of the contaminating air will be dissolved into the sample water. However, even with near-total dissolution of the modern-air derived CO_2, the contributions to DIC are only 1.3-53 nM, in comparison to native DIC 430-2400 μM analyzed in fracture water samples, and thus any modern ^{14}C added through air-contamination will not affect the measured $^{14}C_{DIC}$ at the per mil level or higher. If the DIC were assumed to be ^{14}C dead, then $\delta^{14}C_{calc}$ is -1000 ‰ at 3 s.f. This result is reflective of the weak leverage that adding a fixed volume of air can have on the sample ^{14}C content and indicates small additions of air to an otherwise closed sampling system is not a sufficient explanation of active ^{14}C concentrations in any sample.

If sampled waters were even briefly exposed to open air, partial isotopic equilibration with atmospheric CO_2 could lead to apparent ^{14}C concentrations up to at least a few percent of modern (R. Yokochi, personal communication). Such an effect would reasonably explain low levels of ^{14}C in MM51940 without the addition of any modern water being required. The fact that CH_4 in MM51940, which was generated in the fracture environment, features lower concentrations of ^{14}C than the coexisting DIC at levels close to zero (Simkus *et al*., 2016), provides further evidence that the source of ^{14}C is from modern inorganic carbon. Although this provides a feasible explanation we cannot test it through simple comparison to air contamination in the noble gas samples analysed in this study. However, we conclude from the above discussion that on balance, the potential pathways for additions of small concentrations of active ^{14}C such as present in a geologically old sample like MM51940 are numerous, and far more plausible than an alternative scenario whereby kyr-age fracture waters somehow accumulated massive excesses of radiogenic noble gases in a manner explainable only with unphysical source terms.

Table 1

Noble gas concentrations of South African fracture fluid gas samples

Sample	Mine	Geology	Depth $km_{b.s.}$	[^{4}He]	[^{20}Ne] [10^{-7}]	[^{36}Ar] [10^{-6}]	[^{86}Kr] [10^{-8}]	[^{130}Xe] [10^{-10}] [cm^{3}STP cm^{-3}STP gas]
MM51940	Masimong	Witwatersrand	1.900	0.1023 (±0.0009)	6.91 (±0.06)	3.42 (±0.02)	3.43 (±0.02)	8.15 (±0.05)
TT107	Tau Tona	Witwatersrand	3.048	0.0418 (±0.0008)	42.4 (±0.7)	18.11 (±0.06)	17.2 (±0.3)	45.1 (±0.8)
SD15	Star Diamonds	Witwatersrand	0.640	0.0092 (±0.0002)	126 (±3)	23.0 (±0.5)	14.0 (±0.3)	23.8 (±0.6)
NO14	Zondereinde	Bushveld	2.100	0.0494 (±0.0009)	90 (±2)	29.1 (±0.5)	23.9 (±0.4)	54.5 (±1.0)
DR5IPC	Driefontein	Transvaal	1.046	0.0032 (±0.0002)	12.1 (±0.2)	4.79 (±0.08)	4.14 (±0.07)	8.1 (±0.1)

Reported errors are 1 σ.

Table 2

Major volatile compositional and stable isotope data and water stable isotope data from South African fluid fracture samples

Sample	N$_2$	O$_2$	H$_2$	CH$_4$	C$_2$H$_6$	C$_3$H$_8$ Vol. %	δ^{18}O (H$_2$O)	δD (H$_2$O) ‰
MM51940	14.7 (13.6)	1.06 (0.15) [0.02]*	b.d.l. (0.0018)	76.6 (82.25)	0.06	b.d.l.	-7.00	-40.06
TT107	64.2 (38.9)	16.2 (0.96) [0.04]	b.d.l.(0.11)	16 (54.96)	0.87	0.13	-4.78	-24.4
SD15	61.7 (60.5)	14.6 (14.4) [0.31]	b.d.l. (0.0004)	19.8 (20.84)	b.d.l.	b.d.l.	-6.27	-38.6
NO14	85.6 (78.6)	0 (0.05) [<0.20]	1.26 (0.27)	12 (16.7)	b.d.l.	b.d.l.	-4.56	-25.0
DR5IPC	75.7 (75.25)	21.3 (19.11)[0.15]	b.d.l. (0.000434)	1.77 (1.93)	0.002	b.d.l.	-4.44	-24.3

*The equivalent % O$_2$ present in the headspace based upon the dissolved O$_2$ measured in the fracture fluid at the borehole corrected for the gas/water flow rate and Henry's Law solubility constant at the *in situ* temperature.

Table 3

He, Ne, and Ar isotope data from South African fracture fluid gas samples

Sample	^{3}He/^{4}He (R$_a$)	^{20}Ne/^{22}Ne	^{21}Ne/^{22}Ne	^{40}Ar/^{36}Ar	^{38}Ar/^{36}Ar
MM51940	0.0161 (±0.0005)	9.047 (±0.007)	0.0643 (±0.0003)	2663 (±4)	0.1859 (±0.0007)
TT107	0.0096 (±0.0004)	9.785 (±0.003)	0.0335 (±0.0001)	449.5 (±0.5)	0.1911 (±0.0005)
SD15	0.0221 (±0.0006)	9.821 (±0.003)	0.0293 (±0.0001)	370.4 (±0.4)	0.1869 (±0.0005)
NO14	0.114 (±0.003)	9.811 (±0.002)	0.0300 (±0.0001)	345.3 (±0.4)	0.1894 (±0.0005)
DR5IPC	0.00115 (±0.0003)	10.08 (±0.01)	0.0306 (±0.0001)	326.9 (±0.5)	0.1828 (±0.0005)

Reported errors are 1 σ.

Table 4

Kr isotope data from South African fracture fluid gas samples.

Sample	^{78}Kr/^{84}Kr	^{80}Kr/^{84}Kr	^{82}Kr/^{84}Kr	^{83}Kr/^{84}Kr	^{86}Kr/^{84}Kr
MM51940	0.00622 (±0.00002)	0.03932 (±0.00005)	0.2014 (±0.0002)	0.2008 (±0.0003)	0.3064 (±0.0004)
TT107	N/A	N/A	N/A	N/A	N/A
SD15	0.00619 (±0.00002)	0.03943 (±0.00004)	0.2018 (±0.0001)	0.2011 (±0.0002)	0.3056 (±0.0003)
NO14	0.00617 (±0.00002)	0.03953 (±0.00003)	0.2019 (±0.00009)	0.2012 (±0.0002)	0.3050 (±0.0003)
DR5IPC	0.00633 (±0.00002)	0.03952 (±0.00005)	0.2020 (±0.0002)	0.2009 (±0.0003)	0.3042 (±0.0004)

N/A: No data reported. Reported errors are 1 σ.

Table 5

Xe isotope data from South African fracture fluid gas samples

Sample	^{124}Xe/^{130}Xe	^{126}Xe/^{130}Xe	^{128}Xe/^{130}Xe	^{129}Xe/^{130}Xe	^{131}Xe/^{130}Xe	^{132}Xe/^{130}Xe	^{134}Xe/^{130}Xe	^{136}Xe/^{130}Xe
MM51940a	0.02336 (±0.00015)	0.02190 (±0.00017)	0.4740 (±0.0018)	6.495 (±0.014)	5.225 (±0.012)	6.706 (±0.010)	2.687 (±0.006)	2.326 (±0.005)
MM51940b	0.02337 (±0.00013)	0.02066 (±0.00014)	0.4727 (±0.0016)	6.511 (±0.020)	5.223 (±0.017)	6.695 (±0.015)	2.696 (±0.009)	2.325 (±0.007)
TT107a	0.02338 (±0.00012)	0.02177 (±0.00016)	0.4723 (±0.0010)	6.496 (±0.013)	5.212 (±0.011)	6.610 (±0.007)	2.564 (±0.006)	2.178 (±0.004)
TT107b	0.02338 (±0.00017)	0.02152 (±0.00032)	0.4735 (±0.0024)	6.522 (±0.041)	5.216 (±0.022)	6.640 (±0.029)	2.615 (±0.028)	2.212 (±0.034)
SD15	0.02357 (±0.00014)	0.02194 (±0.00015)	0.4719 (±0.0015)	6.493 (±0.019)	5.210 (±0.016)	6.613 (±0.013)	2.578 (±0.008)	2.194 (±0.006)
NO14a	0.02336 (±0.00015)	0.02184 (±0.00020)	0.4728 (±0.0012)	6.488 (±0.016)	5.214 (±0.014)	6.619 (±0.009)	2.565 (±0.007)	2.179 (±0.005)
NO14b	0.02313 (±0.00056)	0.02217 (±0.0003)	0.4706 (±0.0030)	6.485 (±0.030)	5.218 (±0.023)	6.623 (±0.020)	2.579 (±0.019)	2.183 (±0.012)
DR5IPC	0.02320 (±0.00017)	0.02161 (±0.00018)	0.4723 (±0.0018)	6.5024 (±0.020)	5.207 (±0.018)	6.610 (±0.014)	2.570 (±0.009)	2.183 (±0.007)

Where duplicate samples are listed, a denotes samples analysed on GVI Helix, and b denotes samples analysed on Thermo Argus VI. GVI Helix results are used for interpretation of all duplicated samples.
Reported errors are 1 σ.

Table 6

Apparent noble gas concentrations of South African fracture fluid gas samples

Sample	F_{water} [L/min]	F_{gas} [L/min]	$[^4He]$ $[10^{-4}]$	$[^{20}Ne]$ $[10^{-7}]$	$[^{36}Ar]$ $[10^{-6}]$	$[^{86}Kr]$ $[10^{-8}]$	$[^{130}Xe]$ $[10^{-8}]$ [cm^{3}STP g^{-1} water]
[‡]Lake Baikal air saturated water at 20 ºC, 1013 mbar			0.000447	1.67	1.05	1.21	0.0387
MM51940	8.0	1.8	240 (±2)	1.62 (±0.01)	0.810 (±0.005)	0.806 (±0.005)	0.0192 (±0.0001)
TT107	3.0	0.1	13.9 (±0.3)	1.41 (±0.02)	0.609 (±0.002)	0.573 (±0.010)	0.0150 (±0.0003)
SD15	7.5	N/A	* 92 (±2)	* 126 (±3)	* 23.2 (±0.5)	* 14.0 (±0.3)	* 0.238 (±0.006)
NO14	6.0	0.1	8.2 (±0.2)	1.50 (±0.03)	0.489 (±0.009)	0.398 (±0.007)	0.0091 (±0.0002)
DR5IPC	13.1	0.0316	0.077 (±0.004)	0.0291 (±0.0005)	0.0117 (±0.0002)	0.0100 (±0.002)	0.000195 (±0.000003)

Note that reported water concentrations are apparent concentrations, generated using flow rates. N/A: Data not available. *Concentrations in sample gas [cm^{3}STP cm^{-3}STP gas]. [‡]Air saturated water data from Kipfer *et al*. (2002). Reported errors are 1 σ.

Table 7

Reconstructed noble gas concentrations and radiogenic isotope ratios of South African fracture fluid samples

Sample	$[^4He]$ $[10^{-4}]$ [cm^{3}STP g^{-1} water]	$[^{20}Ne]$ $[10^{-7}]$	$[^{36}Ar]$ $[10^{-6}]$	$[^{86}Kr]$ $[10^{-8}]$	$[^{130}Xe]$ $[10^{-8}]$	$^{21}Ne/^{22}Ne$	$^{40}Ar/^{36}Ar$	$^{136}Xe/^{130}Xe$
[‡]ASW	0.000447	1.67	1.05	1.21	0.0387			
MM51940	326 (±7)	1.69 (±0.04)	1.05	1.16 (±0.02)	0.0300 (±0.0006)	0.00846 (±0.00019)	2873 (±61)	2.331 (±0.049)
TT107	20.1 (±0.5)	1.74 (±0.05)	1.05	1.27 (±0.03)	0.0424 (±0.001)	0.00349 (±0.00009)	454 (±9)	2.178 (±0.057)
NO14	14.6 (±0.4)	1.63 (±0.04)	1.05	1.29 (±0.03)	0.041 (±0.001)	0.00309 (±0.00008)	346 (±9)	2.179 (±0.059)
DR5IPC	8.2 (±0.5)	1.69 (±0.04)	1.05	1.05 (±0.03)	0.0242 (±0.0006)	0.00310 (±0.00008)	333 (±9)	2.183 (±0.059)

[‡]ASW data from Kipfer *et al*. (2002). Reported errors are 1 σ.

Table 8

Radiogenic noble gas concentrations, and residence times of South African fracture fluid samples

Sample	$[^4He^*]$ $[10^{-4}]$	$[^{21}Ne^*]$ $[10^{-10}]$	$[^{40}Ar^*]$ $[10^{-4}]$	$[^{136}Xe^*]$ $[10^{-12}]$	Closed system ages				Open system ages			
					$^4He^*$	$^{21}Ne^*$	$^{40}Ar^*$	$^{136}Xe^*$	$^4He^*$	$^{21}Ne^*$	$^{40}Ar^*$	$^{136}Xe^*$
				$[cm^3STP\ g^{-1}\ water]$				[Myr]				[Myr]
MM51940	326 (±8)	9.3 (±0.4)	27.0 (±0.6)	46 (±2)	97 (±44)	62 (±29)	95 (±43)	40 (±18)	10.8 (±4.9)	7.7 (±3.6)	4.7 (±2.1)	3.4 (±1.5)
TT107	20.1 (±0.5)	0.91 (±0.04)	1.64 (±0.03)	8.85 (±0.04)	6.0 (±2.7)	6.1 (±2.9)	5.7 (±2.6)	0.77 (±0.35)	1.0 (±0.4)	1.2 (±0.6)	0.45 (±0.20)	0.10 (±0.45)
NO14	14.6 (±0.4)	0.86 (±0.03)	0.50 (±0.01)	1.21 (±0.05)	9.1 (±4.1)	12.0 (±5.6)	3.8 (±1.7)	2.7 (±1.2)	0.035 (±0.016)	0.047 (±0.022)	0.0060 (±0.0027)	0.0062 (±0.0029)
DR5IPC	8.23 (±0.47)	N/A	0.359 (±0.01)	1.74 (±0.08)	2.6 (±1.2)	N/A	12.0 (±5.4)	1.1 (±0.5)	0.69 (±0.31)	N/A	0.20 (±0.09)	0.31 (±0.14)

Sample SD15 is omitted due to overwhelming air contamination. N/A: No age calculated. Ages calculated from ^{136}Xe use results from analyses on the GVI instrument for all samples except DR5IPC, where ^{136}Xe was only analysed with the Argus VI instrument.

Table 9

Model ^{14}C ages, and open-system flux terms, for South African fracture fluid samples

Sample	$[^4He^*]$ $[10^{-4}]$	$[^{40}Ar^*]$ $[10^{-4}]$	Model ^{14}C age	Host rock radioelement concentration			Calculated open-system crustal flux		J_{4He}/J_{4He}^{AUC}	J_{40Ar}/J_{40Ar}^{AUC}
		$[cm^3STP\ g^{-1}\ water]$	[kyr]	[Th]	[U] [ppm]	[K] [wt %]	J_{4He}	J_{40Ar} $[cm^3STP\ cm^{-2}\ yr^{-1}]$		
Average Upper Crust (AUC)				10.6[1]	2.8[1]	3.4[1]	$3.6 \times 10^{-6\,[2]}$	$7.3 \times 10^{-7\,[1,2]}$	1	1
MM51940	328 (±8)	328 (±8)	32.1	10.9[4]	4.7[5]	1.91[4]	1.37×10^{-3}	1.13×10^{-4}	380	150
TT107	20.1 (±0.5)	1.64 (±0.03)	1.41-5.68[3]	10.9[4]	4.7[5]	1.91[4]	$7.6\text{-}31 \times 10^{-4}$	$6.2\text{-}25 \times 10^{-5}$	210-850	85-340
NO14	14.6 (±0.4)	0.49 (±0.0006)	4.00	0.41[6]	0.11[6]	0.054[6]	3.2×10^{-5}	1.1×10^{-6}	8.9	1.5
DR5IPC	8.23 (±0.47)	0.359 (±0.01)	16.4-22.9[3]	5.0[4]	17.6[5]	0.56[4]	$1.5\text{-}2.0 \times 10^{-4}$	$6.4\text{-}9.0 \times 10^{-6}$	40-57	8.8-12

External fluxes are calculated to give agreement between radiogenic noble gas and model ^{14}C residence times. [1]Taylor and McLennan (1985); [2]Torgersen and Clarke (1985); [3]Simkus *et al.* (2016); [4]Nicolaysen *et al.* (1981); [5]Lippmann *et al.* (2003); [6]Lee (1983).

Table 10

Water isotope, radiogenic noble gas, and closed-system residence time data for Welkom District fracture fluids

Sample	$\delta^{18}O$ (H$_2$O)	δD (H$_2$O)	$[^4He^*]$ $[10^{-4}]$	$[^{40}Ar^*]$ $[10^{-4}]$	$[^{136}Xe^*]$ $[10^{-12}]$	Closed system ages[ǂ]		
	‰				$[cm^3STP\ g^{-1}\ water]$	$^4He^*$	$^{40}Ar^*$	$^{136}Xe^*$ [Myr]
MM51940[1]	-7.00	-40.06	328 (±8)	27.0 (±0.6)	46 (±2)	97 (±44)	95 (±43)	40 (±18)
BE16#1[2]	-5.85	-42.3	319 (±52)	16.8 (±2.2)	30 (±38)	95 (±45)	60 (±28)	30 (±41)
BE23[2]	-6.17	-41.0	129 (±5)	10.9 (±1.1)	14 (±17)	39 (±17)	39 (±18)	13 (±20)
BE24#2[2]	-6.13	-42.7	142 (±8)	12.7 (±1.6)	20 (±15)	42 (±19)	45 (±21)	15 (±21)
BE325[2]	-6.71	-43.2	457 (±70)	30.4 (±3.6)	27 (±33)	136 (±64)	107 (±50)	26 (±15)
BE327[2]	-6.66	-41.2	323 (±32)	19.2 (±2.0)	28 (±16)	96 (±44)	68 (±32)	31 (±19)
MM519870[3]	-6.52[3]	-37.96[3]	274 (±14)[4]	18.5 (±0.5)[4]	45 (±2)[4]	81 (±37)	66 (±30)	39 (±18)

[ǂ]Closed system residence times of all samples are calculated using the same model parameters as for MM51940 in Table. [1]This study. [2]Lippmann *et al.* (2003) Tables 3, 5. [3]Onstott *et al.* (2006) Appendix. [4]Calculated using radiogenic isotope ratios in Lippmann-Pipke *et al.* (2011) and degassing-corrected atmospheric noble gas concentrations for MM51940 from this study.

References

Andrews, J.N., Davis, S.N., Fabryka-Martin, J., Fontes, J.-C., Lehmann, B.E., Loosli, H.H., Michelot, J.-L., Moser, H., Smith, B., Wolf, M., 1989. The in situ production of radioisotopes in rock matrices with particular reference to the Stripa granite. Geochim. Cosmochim. Acta 53, 1803–1815. https://doi.org/10.1016/0016-7037(89)90301-3

Ballentine, C.J., Burgess, R., Marty, B., 2002. Tracing Fluid Origin, Transport and Interaction in the Crust. Rev. Mineral. Geochem. 47, 539–614. https://doi.org/10.2138/rmg.2002.47.13

Ballentine, C.J., Burnard, P.G., 2002. Production, Release and Transport of Noble Gases in the Continental Crust. Rev. Mineral. Geochem. 47, 481–538. https://doi.org/10.2138/rmg.2002.47.12

Ballentine, C.J., Sherwood Lollar, B., 2002. Regional groundwater focusing of nitrogen and noble gases into the Hugoton-Panhandle giant gas field, USA. Geochim. Cosmochim. Acta 66, 2483–2497. https://doi.org/10.1016/S0016-7037(02)00850-5

Barry, P.H., Lawson, M., Meurer, W.P., Warr, O., Mabry, J.C., Byrne, D.J., Ballentine, C.J., 2016. Noble gases solubility models of hydrocarbon charge mechanism in the Sleipner Vest gas field. Geochim. Cosmochim. Acta 194, 291–309. https://doi.org/10.1016/j.gca.2016.08.021

Basford, J.R., Bradley, J.G., Dragon, J.C., Pepin, R.O., Coscio, M.R., Murthy, V.R., 1973. Krypton and Xenon in Lunar Fines. Proceeding Fourth Lunar Sci. Conf. 2, 1915–1955.

Besse, J., Courtillot, V., 1988. Paleogeographic maps of the continents bordering the Indian Ocean since the Early Jurassic. J. Geophys. Res. Solid Earth 93, 11791–11808. https://doi.org/10.1029/JB093iB10p11791

Bomberg, M., Lamminmäki, T., Itävaara, M., 2016. Microbial communities and their predicted metabolic characteristics in deep fracture groundwaters of the crystalline bedrock at Olkiluoto, Finland. Biogeosciences 13, 6031–6047. https://doi.org/10.5194/bg-13-6031-2016

Bomberg, M., Nyssö, Nen, M., Pitkä, Nen, P., Lehtinen, A., Itä, Vaara, M., 2015. Active Microbial Communities Inhabit Sulphate-Methane Interphase in Deep Bedrock Fracture Fluids in Olkiluoto, Finland. BioMed Res. Int. 2015, e979530. https://doi.org/10.1155/2015/979530

Borgonie, G., Linage-Alvarez, B., Ojo, A.O., Mundle, S.O.C., Freese, L.B., Rooyen, C.V., Kuloyo, O., Albertyn, J., Pohl, C., Cason, E.D., Vermeulen, J., Pienaar, C., Litthauer, D., Niekerk, H.V., Eeden, J.V., Lollar, B.S., Onstott, T.C., Heerden, E.V., 2015. Eukaryotic opportunists dominate the deep-subsurface biosphere in South Africa. Nat. Commun. 6, 8952. https://doi.org/10.1038/ncomms9952

Braun, J., Guillocheau, F., Robin, C., Baby, G., Jelsma, H., 2014. Rapid erosion of the Southern African Plateau as it climbs over a mantle superswell. J. Geophys. Res. Solid Earth 119, 2014JB010998. https://doi.org/10.1002/2014JB010998

Cawthorn, R.G., 2010. The Platinum Group Element Deposits of the Bushveld Complex in South Africa. Platin. Met. Rev. 54, 205–215.

Chivian, D., Brodie, E.L., Alm, E.J., Culley, D.E., Dehal, P.S., DeSantis, T.Z., Gihring, T.M., Lapidus, A., Lin, L.-H., Lowry, S.R., Moser, D.P., Richardson, P.M., Southam, G., Wanger, G., Pratt, L.M., Andersen, G.L., Hazen, T.C., Brockman, F.J., Arkin, A.P., Onstott, T.C., 2008. Environmental Genomics Reveals a Single-Species Ecosystem Deep Within Earth. Science 322, 275–278. https://doi.org/10.1126/science.1155495

Coleman, M.L., Shepherd, T.J., Durham, J.J., Rouse, J.E., Moore, G.R., 1982. Reduction of water with zinc for hydrogen isotope analysis. Anal. Chem. 54, 993–995. https://doi.org/10.1021/ac00243a035

Craig, H., 1961. Isotopic Variations in Meteoric Waters. Science 133, 1702–1703. https://doi.org/10.1126/science.133.3465.1702

Dansgaard, W., 1964. Stable isotopes in precipitation. Tellus 16, 436–468. https://doi.org/10.1111/j.2153-3490.1964.tb00181.x

Duane, M.J., Pigozzi, G., Harris, C., 1997. Geochemistry of some deep gold mine waters from the western portion of the Witwatersrand Basin, South Africa. J. Afr. Earth Sci. 24, 105–123. https://doi.org/10.1016/S0899-5362(97)00030-4

Eberhardt, P., Eugster, O., Marti, K., 1965. Notizen: A Redetermination of the Isotopic Composition of Atmospheric Neon. Z. Für Naturforschung A 20, 623–624. https://doi.org/10.1515/zna-1965-0420

Eikenberg, J., Signer, P., Wieler, R., 1993. U-Xe, U-Kr, and U-Pb systematics for dating uranium minerals and investigations of the production of nucleogenic neon and argon. Geochim. Cosmochim. Acta 57, 1053–1069. https://doi.org/10.1016/0016-7037(93)90040-4

Epstein, S., Mayeda, T., 1953. Variation of O18 content of waters from natural sources. Geochim. Cosmochim. Acta 4, 213–224. https://doi.org/10.1016/0016-7037(53)90051-9

Field, M., Stiefenhofer, J., Robey, J., Kurszlaukis, S., 2008. Kimberlite-hosted diamond deposits of southern Africa: A review. Ore Geol. Rev., The Genesis of Gem Deposits 34, 33–75. https://doi.org/10.1016/j.oregeorev.2007.11.002

Frape, S.K., Fritz, P., McNutt, R.H., 1984. Water-rock interaction and chemistry of groundwaters from the Canadian Shield. Geochim. Cosmochim. Acta 48, 1617–1627. https://doi.org/10.1016/0016-7037(84)90331-4

Fritz, P., Frape, S.K., 1982. Saline groundwaters in the Canadian Shield — A first overview. Chem. Geol., Geochemistry of Radioactive Waste Disposal 36, 179–190. https://doi.org/10.1016/0009-2541(82)90045-6

Gihring, T.M., Moser, D.P., Lin, L.-H., Davidson, M., Onstott, T.C., Morgan, L., Milleson, M., Kieft, T.L., Trimarco, E., Balkwill, D.L., Dollhopf, M.E., 2006. The Distribution of Microbial Taxa in the Subsurface Water of the Kalahari Shield, South Africa. Geomicrobiol. J. 23, 415–430. https://doi.org/10.1080/01490450600875696

Holland, G., Cassidy, M., Ballentine, C.J., 2009. Meteorite Kr in Earth's Mantle Suggests a Late Accretionary Source for the Atmosphere. Science 326, 1522–1525. https://doi.org/10.1126/science.1179518

Holland, G., Lollar, B.S., Li, L., Lacrampe-Couloume, G., Slater, G.F., Ballentine, C.J., 2013. Deep fracture fluids isolated in the crust since the Precambrian era. Nature 497, 357–360. https://doi.org/10.1038/nature12127

IAEA/WMO, 2002. Global Network for Isotopes in Precipitation [WWW Document]. GNIP Database. URL https://nucleus.iaea.org/wiser/gnip (accessed 2.13.17).

Kennedy, B.M., Hiyagon, H., Reynolds, J.H., 1990. Crustal neon: a striking uniformity. Earth Planet. Sci. Lett. 98, 277–286. https://doi.org/10.1016/0012-821X(90)90030-2

Kietäväinen, R., Ahonen, L., Kukkonen, I.T., Niedermann, S., Wiersberg, T., 2014. Noble gas residence times of saline waters within crystalline bedrock, Outokumpu Deep Drill Hole, Finland. Geochim. Cosmochim. Acta 145, 159–174. https://doi.org/10.1016/j.gca.2014.09.012

Kipfer, R., Aeschbach-Hertig, W., Peeters, F., Stute, M., 2002. Noble Gases in Lakes and Ground Waters. Rev. Mineral. Geochem. 47, 615–700. https://doi.org/10.2138/rmg.2002.47.14

Lau, M.C.Y., Cameron, C., Magnabosco, C., Brown, C.T., Schilkey, F., Grim, S., Hendrickson, S., Pullin, M., Sherwood Lollar, B., van Heerden, E., Kieft, T.L., Onstott, T.C., 2014. Phylogeny and phylogeography of functional genes shared among seven terrestrial subsurface metagenomes reveal N-cycling and microbial evolutionary relationships. Front. Microbiol. 5. https://doi.org/10.3389/fmicb.2014.00531

Lau, M.C.Y., Kieft, T.L., Kuloyo, O., Linage-Alvarez, B., Heerden, E. van, Lindsay, M.R., Magnabosco, C., Wang, W., Wiggins, J.B., Guo, L., Perlman, D.H., Kyin, S., Shwe, H.H., Harris, R.L., Oh, Y., Yi, M.J., Purtschert, R., Slater, G.F., Ono, S., Wei, S., Li, L., Lollar, B.S., Onstott, T.C., 2016. An oligotrophic deep-subsurface community dependent on syntrophy is dominated by sulfur-driven autotrophic denitrifiers. Proc. Natl. Acad. Sci. 113, E7927–E7936. https://doi.org/10.1073/pnas.1612244113

Lee, C.A., 1983. Trace and platinum-group element geochemistry and the development of the Merensky unit of the Western Bushveld complex. Miner. Deposita 18, 173–190. https://doi.org/10.1007/BF00206207

Lee, J.-Y., Marti, K., Severinghaus, J.P., Kawamura, K., Yoo, H.-S., Lee, J.B., Kim, J.S., 2006. A redetermination of the isotopic abundances of atmospheric Ar. Geochim. Cosmochim. Acta 70, 4507–4512. https://doi.org/10.1016/j.gca.2006.06.1563

Lin, L.-H., Wang, P.-L., Rumble, D., Lippmann-Pipke, J., Boice, E., Pratt, L.M., Lollar, B.S., Brodie, E.L., Hazen, T.C., Andersen, G.L., DeSantis, T.Z., Moser, D.P., Kershaw, D., Onstott, T.C., 2006. Long-Term Sustainability of a High-Energy, Low-Diversity Crustal Biome. Science 314, 479–482. https://doi.org/10.1126/science.1127376

Lippmann, J., Stute, M., Torgersen, T., Moser, D.P., Hall, J.A., Lin, L., Borcsik, M., Bellamy, R.E.S., Onstott, T.C., 2003. Dating ultra-deep mine waters with noble gases and 36Cl, Witwatersrand Basin, South Africa. Geochim. Cosmochim. Acta 67, 4597–4619. https://doi.org/10.1016/S0016-7037(03)00414-9

Lippmann-Pipke, J., Sherwood Lollar, B., Niedermann, S., Stroncik, N.A., Naumann, R., van Heerden, E., Onstott, T.C., 2011. Neon identifies two billion year old fluid component in Kaapvaal Craton. Chem. Geol. 283, 287–296. https://doi.org/10.1016/j.chemgeo.2011.01.028

Macintyre, R.M., Dawson, J.B., 1976. Age and significance of some South African kimberlites.

Magnabosco, C., Ryan, K., Lau, M.C.Y., Kuloyo, O., Sherwood Lollar, B., Kieft, T.L., van Heerden, E., Onstott, T.C., 2016. A metagenomic window into carbon metabolism at
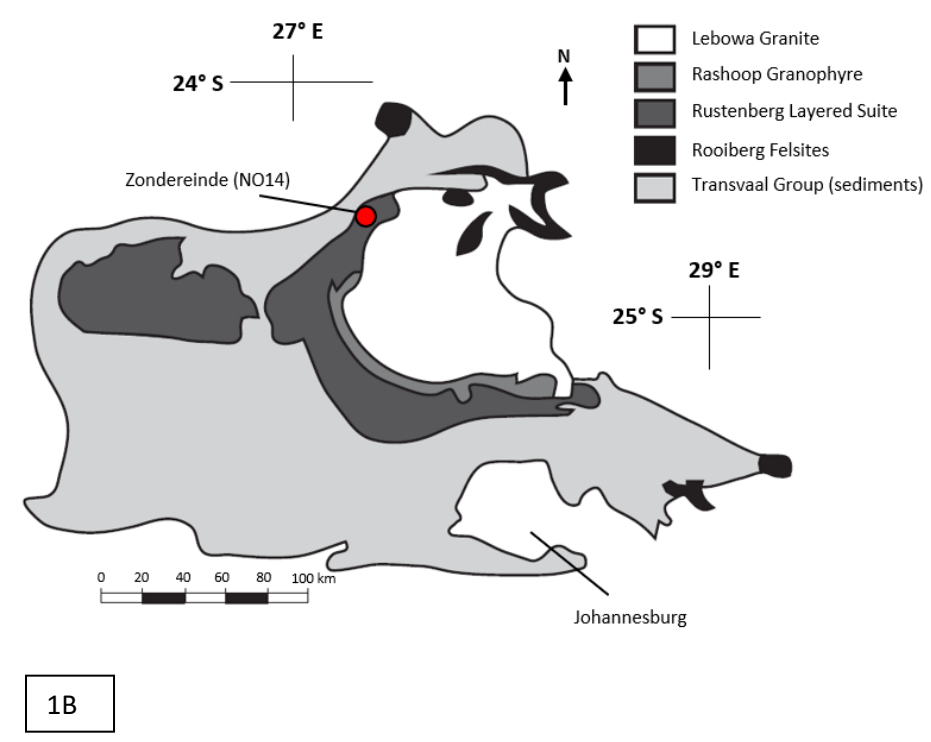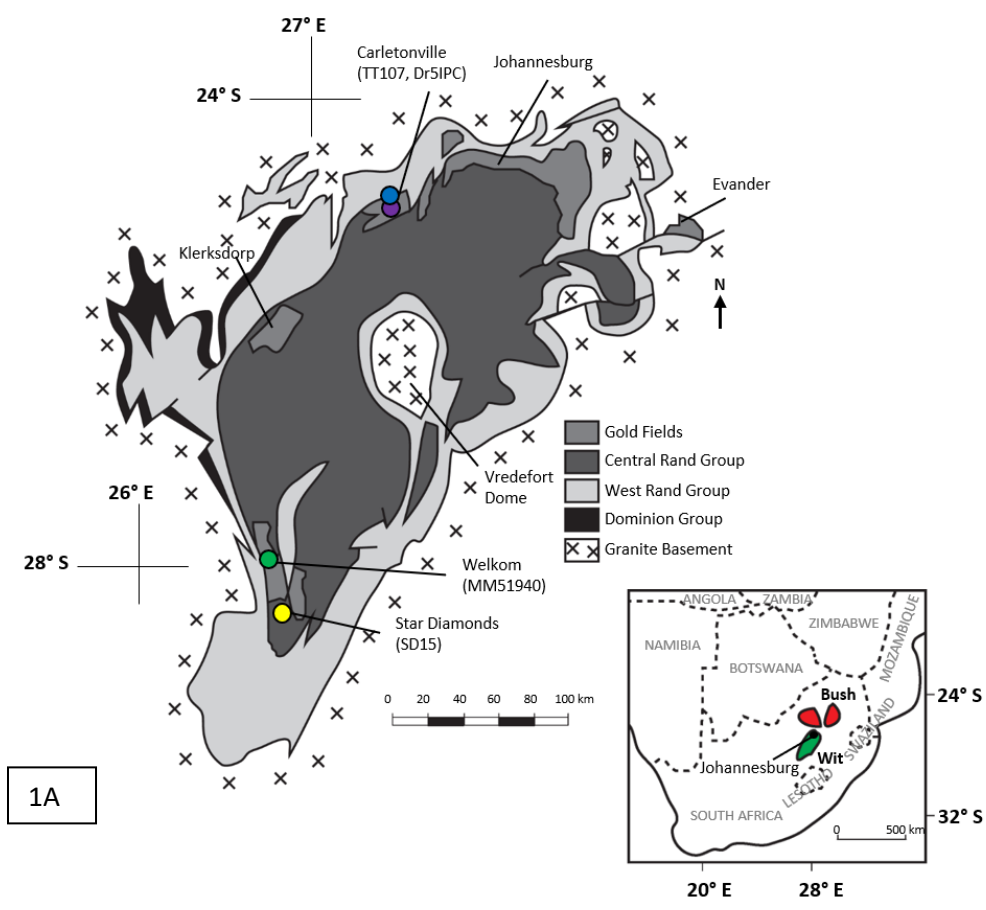
3 km depth in Precambrian continental crust. ISME J. 10, 730–741. https://doi.org/10.1038/ismej.2015.150

Magnabosco, C., Tekere, M., Lau, M.C.Y., Linage, B., Kuloyo, O., Erasmus, M., Cason, E., van Heerden, E., Borgonie, G., Kieft, T.L., Olivier, J., Onstott, T.C., 2014. Comparisons of the composition and biogeographic distribution of the bacterial communities occupying South African thermal springs with those inhabiting deep subsurface fracture water. Front. Microbiol. 5. https://doi.org/10.3389/fmicb.2014.00679

Mamyrin, B.A., Anufriev, G.S., Kamenskiy, I.L., Tolstikhin, I.N., 1970. Determination of the isotopic composition of atmospheric helium. Geochem. Int. 7, 498–505.

Manzi, M., Durrheim, R., Hein, K., King, N., 2012. 3D edge detection seismic attributes used to map potential conduits for water and methane in deep gold mines in the Witwatersrand basin, South Africa. GEOPHYSICS 77, WC133-WC147. https://doi.org/10.1190/geo2012-0135.1

McCandless, T.E., Ruiz, J., 1991. Osmium isotopes and crustal sources for platinum-group mineralization in the Bushveld Complex, South Africa. Geology 19, 1225–1228. https://doi.org/10.1130/0091-7613(1991)019<1225:OIACSF>2.3.CO;2

Nicolaysen, L.O., Hart, R.J., Gale, N.H., 1981. The Vredefort radioelement profile extended to supracrustal strata at Carletonville, with implications for continental heat flow. J. Geophys. Res. Solid Earth 86, 10653–10661. https://doi.org/10.1029/JB086iB11p10653

Nordstrom, D.K., Olsson, T., Carlsson, L., Fritz, P., 1989. Introduction to the hydrogeochemical investigations within the International Stripa Project. Geochim. Cosmochim. Acta 53, 1717–1726. https://doi.org/10.1016/0016-7037(89)90293-7

Nyyssönen, M., Bomberg, M., Kapanen, A., Nousiainen, A., Pitkänen, P., Itävaara, M., 2012. Methanogenic and Sulphate-Reducing Microbial Communities in Deep Groundwater of Crystalline Rock Fractures in Olkiluoto, Finland. Geomicrobiol. J. 29, 863–878. https://doi.org/10.1080/01490451.2011.635759

Nyyssönen, M., Hultman, J., Ahonen, L., Kukkonen, I., Paulin, L., Laine, P., Itävaara, M., Auvinen, P., 2014. Taxonomically and functionally diverse microbial communities in deep crystalline rocks of the Fennoscandian shield. ISME J. 8, 126–138. https://doi.org/10.1038/ismej.2013.125

Onstott, T.C., Lin, L.-H., Davidson, M., Mislowack, B., Borcsik, M., Hall, J., Slater, G., Ward, J., Lollar, B.S., Lippmann-Pipke, J., Boice, E., Pratt, L.M., Pfiffner, S., Moser,

D., Gihring, T., Kieft, T.L., Phelps, T.J., Vanheerden, E., Litthaur, D., Deflaun, M., Rothmel, R., Wanger, G., Southam, G., 2006. The Origin and Age of Biogeochemical Trends in Deep Fracture Water of the Witwatersrand Basin, South Africa. Geomicrobiol. J. 23, 369–414. https://doi.org/10.1080/01490450600875688

Pedersen, K., Bengtsson, A.F., Edlund, J.S., Eriksson, L.C., 2014. Sulphate-controlled Diversity of Subterranean Microbial Communities over Depth in Deep Groundwater with Opposing Gradients of Sulphate and Methane. Geomicrobiol. J. 31, 617–631. https://doi.org/10.1080/01490451.2013.879508

Podosek, F.A., Bernatowicz, T.J., Kramer, F.E., 1981. Adsorption of xenon and krypton on shales. Geochim. Cosmochim. Acta 45, 2401–2415. https://doi.org/10.1016/0016-7037(81)90094-6

Porcelli, D., Ballentine, C.J., Wieler, R., 2002. An Overview of Noble Gas Geochemistry and Cosmochemistry. Rev. Mineral. Geochem. 47, 1–19. https://doi.org/10.2138/rmg.2002.47.1

Pujol, M., Marty, B., Burgess, R., 2011. Chondritic-like xenon trapped in Archean rocks: A possible signature of the ancient atmosphere. Earth Planet. Sci. Lett. 308, 298–306. https://doi.org/10.1016/j.epsl.2011.05.053

Pujol, M., Marty, B., Burnard, P., Philippot, P., 2009. Xenon in Archean barite: Weak decay of 130Ba, mass-dependent isotopic fractionation and implication for barite formation. Geochim. Cosmochim. Acta 73, 6834–6846. https://doi.org/10.1016/j.gca.2009.08.002

Purkamo, L., Bomberg, M., Kietäväinen, R., Salavirta, H., Nyyssönen, M., Nuppunen-Puputti, M., Ahonen, L., Kukkonen, I., Itävaara, M., 2016. Microbial co-occurrence patterns in deep Precambrian bedrock fracture fluids. Biogeosciences 13, 3091–3108. https://doi.org/10.5194/bg-13-3091-2016

Ragettli, R.A., Hebeda, E.H., Signer, P., Wieler, R., 1994. Uranium-xenon chronology: precise determination of $\lambda s f * 136 Y s f$ for spontaneous fission of 238U. Earth Planet. Sci. Lett. 128, 653–670. https://doi.org/10.1016/0012-821X(94)90177-5

Reimold, W.U., Meshik, A.P., Smits, G., Pravdivtseva, O.V., Shukolyukov, Y.A., 1995. Fission xenon dating of Witwatersrand uraninites: Implications for geological activity in the Central Kaapvaal Craton about 1 Ga ago. Geochim. Cosmochim. Acta 59, 5177–5190. https://doi.org/10.1016/0016-7037(95)00354-1

Robb, L.J., Charlesworth, E.G., Drennan, G.R., Gibson, R.L., Tongu, E.L., 1997. Tectono-metamorphic setting and paragenetic sequence of Au-U mineralisation in the
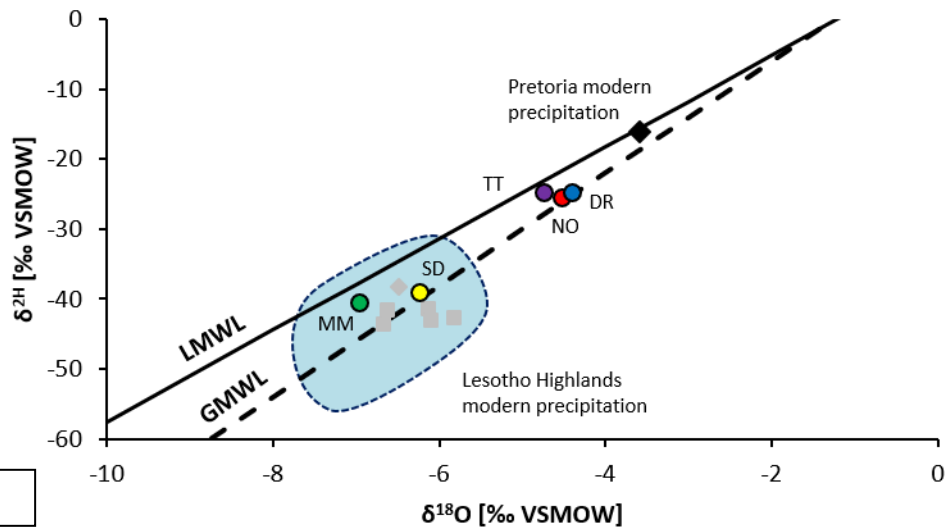
Archaean Witwatersrand Basin, South Africa. Aust. J. Earth Sci. 44, 353–371. https://doi.org/10.1080/08120099708728317

Robb, L.J., Meyer, F.M., 1995. The Witwatersrand Basin, South Africa: Geological framework and mineralization processes. Ore Geol. Rev. 10, 67–94. https://doi.org/10.1016/0169-1368(95)00011-9

Rozanski, K., Araguás-Araguás, L., Gonfiantini, R., 1993. Isotopic Patterns in Modern Global Precipitation, in: Swart, P.K., Lohmann, K.C., Mckenzie, J., Savin, S. (Eds.), Climate Change in Continental Isotopic Records. American Geophysical Union, pp. 1–36. https://doi.org/10.1029/GM078p0001

Scotese, C.R., Boucot, A.J., McKerrow, W.S., 1999. Gondwanan palaeogeography and pal1oclimatology. J. Afr. Earth Sci. 28, 99–114. https://doi.org/10.1016/S0899-5362(98)00084-0

Sherwood Lollar, B., Frape, S.K., Fritz, P., Macko, S.A., Welhan, J.A., Blomqvist, R., Lahermo, P.W., 1993. Evidence for bacterially generated hydrocarbon gas in Canadian shield and fennoscandian shield rocks. Geochim. Cosmochim. Acta 57, 5073–5085. https://doi.org/10.1016/0016-7037(93)90609-Z

Sherwood Lollar, B., Lacrampe-Couloume, G., Slater, G.F., Ward, J., Moser, D.P., Gihring, T.M., Lin, L.-H., Onstott, T.C., 2006. Unravelling abiogenic and biogenic sources of methane in the Earth's deep subsurface. Chem. Geol., Special Issue in Honour of R.K. O'Nions 226, 328–339. https://doi.org/10.1016/j.chemgeo.2005.09.027

Sherwood Lollar, B., Lacrampe-Couloume, G., Voglesonger, K., Onstott, T.C., Pratt, L.M., Slater, G.F., 2008. Isotopic signatures of CH4 and higher hydrocarbon gases from Precambrian Shield sites: A model for abiogenic polymerization of hydrocarbons. Geochim. Cosmochim. Acta 72, 4778–4795. https://doi.org/10.1016/j.gca.2008.07.004

Sherwood Lollar, B., Voglesonger, K., Lin, L.-H., Lacrampe-Couloume, G., Telling, J., Abrajano, T. a., Onstott, T. c., Pratt, L. m., 2007. Hydrogeologic Controls on Episodic H2 Release from Precambrian Fractured Rocks—Energy for Deep Subsurface Life on Earth and Mars. Astrobiology 7, 971–986. https://doi.org/10.1089/ast.2006.0096

Sherwood Lollar, B., Onstott, T.C., Lacrampe-Couloume, G., Ballentine, C.J., 2014. The contribution of the Precambrian continental lithosphere to global H2 production. Nature 516, 379–382. https://doi.org/10.1038/nature14017

Silver, B.J., Raymond, R., Sigman, D.M., Prokopeko, M., Sherwood Lollar, B., Lacrampe-Couloume, G., Fogel, M.L., Pratt, L.M., Lefticariu, L., Onstott, T.C., 2012. The origin

of NO3− and N2 in deep subsurface fracture water of South Africa. Chem. Geol. 294–295, 51–62. https://doi.org/10.1016/j.chemgeo.2011.11.017

Simkus, D.N., Slater, G.F., Lollar, B.S., Wilkie, K., Kieft, T.L., Magnabosco, C., Lau, M.C.Y., Pullin, M.J., Hendrickson, S.B., Wommack, K.E., Sakowski, E.G., Heerden, E. van, Kuloyo, O., Linage, B., Borgonie, G., Onstott, T.C., 2016. Variations in microbial carbon sources and cycling in the deep continental subsurface. Geochim. Cosmochim. Acta 173, 264–283. https://doi.org/10.1016/j.gca.2015.10.003

Sleep, N.H., Zoback, M.D., 2007. Did Earthquakes Keep the Early Crust Habitable? Astrobiology 7, 1023–1032. https://doi.org/10.1089/ast.2006.0091

Steiger, R.H., Jäger, E., 1977. Subcommission on geochronology: Convention on the use of decay constants in geo- and cosmochronology. Earth Planet. Sci. Lett. 36, 359–362. https://doi.org/10.1016/0012-821X(77)90060-7

Taylor, S.R., McLennan, S.M., 1985. The continental crust: Its composition and evolution.

Torgersen, T., Clarke, W.B., 1985. Helium accumulation in groundwater, I: An evaluation of sources and the continental flux of crustal 4He in the Great Artesian Basin, Australia. Geochim. Cosmochim. Acta 49, 1211–1218. https://doi.org/10.1016/0016-7037(85)90011-0

Torsvik, T.H., Cocks, L.R.M., 2013. Gondwana from top to base in space and time. Gondwana Res. 24, 999–1030. https://doi.org/10.1016/j.gr.2013.06.012

Torsvik, T.H., Voo, R.V. der, 2002. Refining Gondwana and Pangea palaeogeography: estimates of Phanerozoic non-dipole (octupole) fields. Geophys. J. Int. 151, 771–794. https://doi.org/10.1046/j.1365-246X.2002.01799.x

Tweedie, E.B., 1986. The Evander Goldfield, in: Anhaeusser, C.R., Maske, S. (Eds.), Mineral Deposits of Southern Africa, Geological Society of South Africa. pp. 705–730.

Vegter, J.R., Foster, B.J., 1992. The hydrology of dolomitic formations in the southern and western Transvaal. Int Contrib Hydrogeol 13, 355–376.

von Gruenewaldt, G., Sharpe, M.R., Hatton, C.J., 1985. The Bushveld Complex; introduction and review. Econ. Geol. 80, 803–812. https://doi.org/10.2113/gsecongeo.80.4.803

Ward, J.A., Slater, G.F., Moser, D.P., Lin, L.-H., Lacrampe-Couloume, G., Bonin, A.S., Davidson, M., Hall, J.A., Mislowack, B., Bellamy, R.E.S., Onstott, T.C., Sherwood Lollar, B., 2004. Microbial hydrocarbon gases in the Witwatersrand Basin, South Africa: Implications for the deep biosphere1. Geochim. Cosmochim. Acta, A Special Issue on Microbial Geochemistry 68, 3239–3250. https://doi.org/10.1016/j.gca.2004.02.020
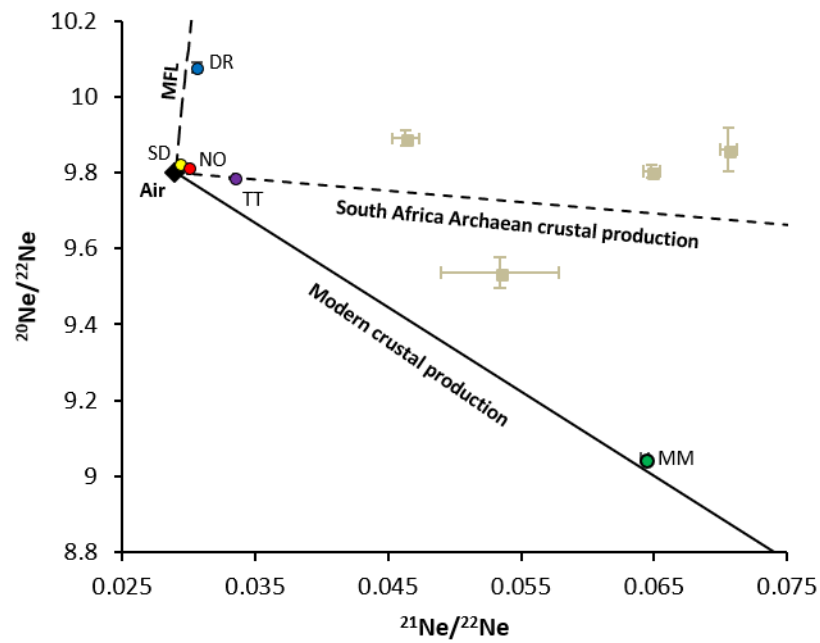
Warr, O., Sherwood Lollar, B., Fellowes, J., Sutcliffe, C.N., McDermott, J.M., Holland, G., Mabry, J.C., Ballentine, C.J., 2018. Tracing ancient hydrogeological fracture network age and compartmentalisation using noble gases. Geochim. Cosmochim. Acta 222, 340–362. https://doi.org/10.1016/j.gca.2017.10.022

West, A.G., February, E.C., Bowen, G.J., 2014. Spatial analysis of hydrogen and oxygen stable isotopes ("isoscapes") in ground water and tap water across South Africa. J. Geochem. Explor. 145, 213–222. https://doi.org/10.1016/j.gexplo.2014.06.009

Wetherill, G.W., 1953. Spontaneous Fission Yields from Uranium and Thorium. Phys. Rev. 92, 907–912. https://doi.org/10.1103/PhysRev.92.907

Yudovskaya, M., Kinnaird, J., Naldrett, A.J., Rodionov, N., Antonov, A., Simakin, S., Kuzmin, D., 2013. Trace-element study and age dating of zircon from chromitites of the Bushveld Complex (South Africa). Mineral. Petrol. 107, 915–942. https://doi.org/10.1007/s00710-013-0269-3

Zhou, Z., Ballentine, C.J., Kipfer, R., Schoell, M., Thibodeaux, S., 2005. Noble gas tracing of groundwater/coalbed methane interaction in the San Juan Basin, USA. Geochim. Cosmochim. Acta 69, 5413–5428. https://doi.org/10.1016/j.gca.2005.06.027
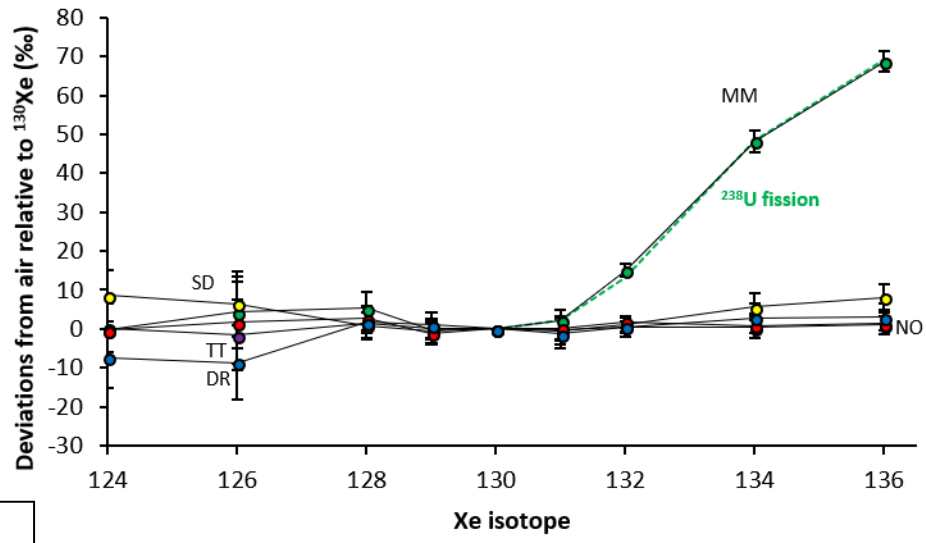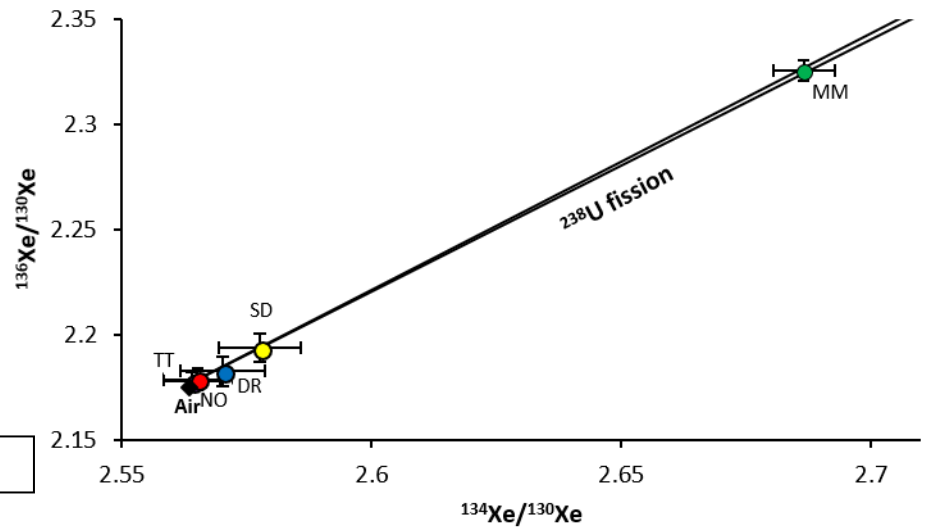
Figure 1A. Geological map showing Gold Fields, Central Rand Group, West Rand Group, Dominion Group, and Granite Basement, with locations Carletonville (TT107, Dr5IPC), Johannesburg, Evander, Klerksdorp, Vredefort Dome, Welkom (MM51940), and Star Diamonds (SD15). Inset map of southern Africa.

Figure 1B. Geological map showing Lebowa Granite, Rashoop Granophyre, Rustenberg Layered Suite, Rooiberg Felsites, and Transvaal Group (sediments), with locations Zondereinde (NO14) and Johannesburg.

2

3

46

4

5

Figure 6

Figure 7A

7D

DR